Chapter 11

Parametric Down-Conversion

Andreas Christ[*], **Alessandro Fedrizzi**[†], **Hannes Hübel**[‡], **Thomas Jennewein**[††], **and Christine Silberhorn**[*]

[*]*Applied Physics, University of Paderborn, Warburger Straße 100, 33098 Paderborn, Germany*
[†]*Centre for Engineered Quantum Systems, Centre for Quantum Computer and Communication Technology, School of Mathematics and Physics, University of Queensland, Brisbane 4072, Australia*
[‡]*Fysikum, University of Stockholm, Roslagstullsbacken 21, 10691 Stockholm, Sweden*
[††]*Institute for Quantum Computing and Department of Physics & Astronomy, University of Waterloo, Waterloo, Canada N2L 3G1*

Chapter Outline

Single-Photon Generation and Detection, Volume 45. http://dx.doi.org/10.1016/B978-0-12-387695-9.00011-1

11.1 INTRODUCTION

Parametric down-conversion (PDC) is a nonlinear process in which a photon from a strong pump laser is converted into two daughter photons under conservation of energy and momentum. Despite its many contenders discussed elsewhere in this book, PDC is still the most widely used technique for generating single photons. The reasons are that PDC is well understood, simple to implement, and produces photons in well-defined spatio-temporal modes at high rates.

Photon pairs generated in PDC were first observed in the late 1960s and early 1970s [1–4]. Two decades later, two independent groups started to study the coherence properties of the created single photons: Shih and Alley [5] realized that the photon pairs could be used to investigate *fundamental* problems in quantum mechanics, such as John Wheeler's delayed choice Gedankenexperiment, or the Einstein-Podolsky-Rosen paradox. Meanwhile, Ghosh, and Mandel observed non-classical interference effects between down-converted photons [6]. Their work was a direct precursor to a landmark experiment by Hong *et al.* [7], who used non-classical two-photon interference on a beamsplitter to demonstrate that PDC photons were created within at least sub-picosecond time intervals. The so-called Hong-Ou-Mandel dip, a drop in coincident photon detection at the output of the beamsplitter as a function of photon arrival time, firmly established PDC as an experimental tool in quantum optics and has since been the key mechanism for many quantum information processing protocols.

The biggest boost of PDC as a tool was, however, the fact that photon pairs created in this process are naturally entangled. The first bright source of highly entangled photons was demonstrated by Kwiat and co-authors in 1995 [8]. This sparked a host of experiments studying the nature of entanglement, such as Bell tests with space-like separated observers [9], quantum teleportation [10], multi-particle entanglement [11], entanglement-based quantum cryptography [12], and many more.

As these applications evolved, they placed increasing demands on photon sources. The biggest improvement to both pair creation rates and flexibility was due to rapid advances in nonlinear optics, specifically, the development

of periodically-poled crystals. Another major development was waveguide technology. Waveguides confine light fields over relatively large distances in optical materials and thus lead to vastly increased PDC generation rates. They also allow for optical integration of sources, optical circuits, and detectors into small-scale devices. Waveguide PDC is however, compared to the more mature bulk-crystal and periodically-poled PDC sources, still in its infancy and it will take some time to eradicate issues such as coupling losses and pump mode suppression.

We will start with a general theoretic description of parametric down-conversion and then move on to the details of heralding photons with PDC. In particular, we will discuss important concepts such as photon purity and phase-matching. The subsequent sections discuss the practical aspects of generating PDC in bulk crystals, in periodically-poled crystals and in waveguides. The reader will find a list of selected experiments at the end of this chapter (see Fig. 11.32). The list is by no means exhaustive, but should give the reader a flavor of the possible variations in single-photon sources based on PDC.

11.2 SINGLE PHOTONS FROM PDC: THEORY

In this section we review the process of parametric down-conversion as a source of single-photon states.

The overall process is sketched in Figure 11.1. A strong pump field is propagating through a medium possessing a $\chi^{(2)}$ nonlinearity. During this interaction one of the pump photons decays into a photon pair, where we label the individual photons signal and trigger. The trigger photon is subsequently detected to herald the presence of its partner the signal photon, effectively generating a source of heralded single photons. Heralded single-photon states are also analyzed and discussed in this chapter, in the context of early (and less efficient) atomic-cascade sources.

This introductory section mainly concentrates on the theory of heralding single photons from PDC and is structured into four parts. In Section 11.2.1

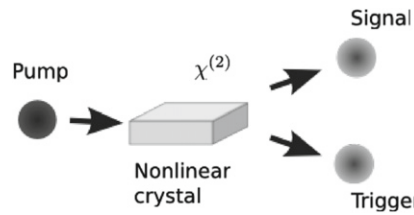

FIGURE 11.1 Single-photon generation using PDC. A pump field is propagating through a medium exhibiting a $\chi^{(2)}$ nonlinearity. During this interaction a pump photon decays into a pair of photons. One of the photons is detected to herald the presence of its partner, effectively creating a heralded single-photon source.

we give an overview of the classical description of PDC and its connection to sum-frequency conversion. In Section 11.2.2 we present a quantum mechanical treatment of PDC and derive the generated two-photon output state. In Section 11.2.3, we elaborate on the process of detecting one photon to herald the presence of its partner and discuss the properties of the heralded signal photon. Finally, in Section 11.2.4 we review the intricacies of heralding pure single-photon Fock states from PDC.

11.2.1 Classical Description of PDC

Although PDC can only be fully described using a quantum mechanical formalisms, it is nevertheless instructional to study a classical form of a nonlinear parametric process like sum-frequency generation. Many of the relations between the classically interacting fields will also hold for the PDC case.

An electro-magnetic field interacting with a dielectric medium will induce a polarization in the material. The normal response of the material is linear, i.e., the incoming electro-magnetic field is not altered in frequency. However at high electric field strengths nonlinear properties cannot be neglected anymore. The polarization P can be expanded in terms of the electro-magnetic field

$$P = \varepsilon_0(\chi^{(1)}E_1 + \chi^{(2)}E_1E_2 + \chi^{(3)}E_1E_2E_3 + \cdots), \tag{11.1}$$

where ε_0 is the vacuum permittivity, $\chi^{(1)}$ is the linear susceptibility, and $\chi^{(2)}, \chi^{(3)}, \ldots$ are the nonlinear susceptibilities of the medium. The nonlinear interaction implies that electro-magnetic waves with different frequencies can interact and, under conservation of energy, frequency conversion can occur. In the $\chi^{(2)}$ process, which is also referred to as three-wave mixing, three electro-magnetic fields interact in a non-centrosymmetric medium and energy can be transferred from one field to another. Since PDC is a three-wave mixing process, the $\chi^{(2)}$ interaction will be discussed in detail here. The higher-order four-wave mixing process with $\chi^{(3)}$ nonlinearities will be discussed in Chapter 12: Four-wave mixing.

The $\chi^{(2)}$ frequency conversion can be roughly divided into two types. The first type has two input fields and produces a single output field. The produced field can have frequencies corresponding to the sum of the input fields, as in sum-frequency generation, or frequencies corresponding to the difference, as in difference-frequency generation. The other type of interaction to which PDC belongs has a single input field that is converted to two output fields, as shown in Fig. 11.1. Historically the resulting fields have been named signal and idler, with the former having the higher frequency. In this book we will refer to the two output fields as *trigger* and *signal*, without specific relation to the frequency. In the quantum mechanical description (Section 11.2.2), PDC gives rise to the spontaneous generation of photon pairs and the presence of a photon in the *trigger* mode heralds the partner photon in the *signal* mode.

The susceptibility $\chi^{(2)}$ is a tensor of rank 3 and its components are defined through the nonlinear part of the polarization and the electric field components in Eq. (11.1)

$$P_i^{\mathrm{NL}} = \varepsilon_0 \sum_{\mathrm{j,k}=1,2,3} \chi_{\mathrm{ijk}} E_{\mathrm{j}} E_{\mathrm{k}}, \tag{11.2}$$

with $i = 1,2,3$. It is customary to assign the cartesian axes x, y, z to the indices values 1, 2, 3. Since the fields E_{j} and E_{k} can be permuted without changing the polarization, the 27 elements of the $\chi^{(2)}$ tensor can be reduced to a matrix with only 18 independent elements d_{ij}

$$\begin{pmatrix} P_{\mathrm{x}} \\ P_{\mathrm{y}} \\ P_{\mathrm{z}} \end{pmatrix} = \varepsilon_0 \begin{pmatrix} d_{11} & d_{12} & d_{13} & d_{14} & d_{15} & d_{16} \\ d_{21} & d_{22} & d_{23} & d_{24} & d_{25} & d_{26} \\ d_{31} & d_{32} & d_{33} & d_{34} & d_{35} & d_{36} \end{pmatrix} \times \begin{pmatrix} E_{\mathrm{x}}^2 \\ E_{\mathrm{y}}^2 \\ E_{\mathrm{z}}^2 \\ 2E_{\mathrm{y}}E_{\mathrm{z}} \\ 2E_{\mathrm{x}}E_{\mathrm{z}} \\ 2E_{\mathrm{x}}E_{\mathrm{y}} \end{pmatrix}. \tag{11.3}$$

The d_{ij} coefficients and other optical properties for some well-known nonlinear crystals are summarized in Fig. 11.33.

If the nonlinear interaction couples pump, trigger, and signal fields with the same polarization, it is referred to as a type-0 interaction. If the pump polarization is orthogonal to the signal and trigger polarization the process is labeled type-I PDC, and if the two output fields are orthogonally polarized the interaction is called type-II PDC.

The additional nonlinear part of the polarization can be added to the macroscopic Maxwell's equations to derive the electric fields. Assuming collinear propagation of the waves along the x-direction the following wave equation is obtained

$$\frac{\partial^2 E}{\partial x^2} = -\mu_0 \left(\varepsilon_0 \frac{\partial^2 E}{\partial t^2} + \frac{\partial^2 P^{\mathrm{NL}}}{\partial t^2} \right). \tag{11.4}$$

In the case of sum-frequency generation, assuming monochromatic fields, two incident plane waves in the form of

$$E_{1,2} = A_{1,2}(x) e^{i(\omega_{1,2} t - k_{1,2} x)}, \tag{11.5}$$

with frequencies ω_1 and ω_2, propagation constants k_1 and k_2, and a possible varying amplitude $A_{1,2}(x)$ along the propagation direction will induce a periodic modulation of the polarization at a frequency of $\omega_3 = \omega_1 + \omega_2$. This, in turn, creates a new field E_3 at frequency ω_3. The solution of the new field can be found from Eq. (11.4) by substituting P^{NL} with the input fields

E_1 and E_2 coupled via $\chi^{(2)}$. The electric field amplitude of E_3 along the propagation direction is then found to be

$$\frac{dA_3}{dx} = \frac{-i\omega_3}{2n_3c} d_{\mathrm{ij}}\, A_1 A_2 e^{i(\Delta k)x}, \tag{11.6}$$

using the slowly varying amplitude approximation $\left(\frac{d^2E}{dx^2} << k\frac{dE}{dx}\right)$. Similar expressions can be derived for the input fields E_1 and E_2. The nonlinear coefficient d_{ij} is derived from the appropriate matrix element in Eq. (11.3) depending on the polarization of the fields. The wave-vector mismatch Δk is given by

$$\Delta k = k_3 - k_1 - k_2 = \frac{n_3\omega_3}{c} - \frac{n_1\omega_1}{c} - \frac{n_2\omega_2}{c}, \tag{11.7}$$

where $n_{\mathrm{j}}, j = 1,2,3$ are refractive indices of the three propagating fields. The amplitude of the generated field after a propagation distance L can readily be found by integrating Eq. (11.6)

$$A_3(L) = \frac{-d_{\mathrm{ij}}\omega_3 A_1 A_2}{2n_3c}\left(\frac{e^{i\Delta kL} - 1}{\Delta k}\right), \tag{11.8}$$

where we assumed that the fields E_1 and E_2 are constant throughout the interaction (the undepleted-pump approximation). The intensity of the E_3 field after length L is obtained by using the relation $I = \frac{1}{2}n\varepsilon_0 cEE^*$ and results in

$$I_3(L) = \frac{d_{\mathrm{ij}}^2\omega_3^2 I_1 I_2 L^2}{2n_1n_2n_3c^3\varepsilon_0}\mathrm{sinc}^2\left(\frac{\Delta kL}{2}\right). \tag{11.9}$$

The efficiency of the conversion process is strongly dependent on the wave-vector mismatch Δk. If $\Delta k \neq 0$, then the generated field becomes out of phase by π after an interaction length of

$$L_{\mathrm{c}} = \frac{\pi}{\Delta k}, \tag{11.10}$$

which is also called the coherence length. At this point the generated field starts to interfere destructively, in effect lowering the conversion efficiency until it reaches zero at $2L_{\mathrm{c}}$. Therefore, it is paramount that the phase-matching condition $\Delta k = 0$ is fulfilled to obtain optimal frequency conversion. Methods of achieving the phase-matching condition are described in the proceeding sections of this chapter. The above derivation strictly holds only for interactions when at least two fields are present, as in sum-frequency generation. In a PDC interaction, however, only the pump field is present and a purely classical treatment cannot explain the creation of the other two fields. In a quantum mechanical picture employing second-quantization formalism discussed in the following section, the zero-point quantum noise gives rise to a field at ω_1 and ω_2. Through the interaction with the pump, the noise fields at ω_1 and ω_2 are amplified via the nonlinear frequency conversion. If the nonlinear interaction is strong, a macroscopic intensity at ω_1 and ω_2 can be observed.

The classical Hamiltonian for the electric field is given by [13]

$$H_{\mathrm{EM}} \propto \int E(r,t) \cdot D(r,t) dr^3. \tag{11.11}$$

By only keeping the 2nd-order nonlinear term in the displacement vector D yields the interaction Hamiltonian for the $\chi^{(2)}$ process

$$H_{\chi^{(2)}} \propto \int \chi^{(2)} E_{\mathrm{p}}(r,t) E_{\mathrm{s}}(r,t) E_{\mathrm{t}}(r,t) dr^3, \tag{11.12}$$

where the subscripts stand for the pump, trigger, and signal fields, respectively.

11.2.2 Quantum Mechanical Description of PDC

Quantizing the electric fields [13] in the Hamiltonian in Eq. (11.12) enables a quantum mechanical description of the process

$$\hat{H}_{\mathrm{PDC}} \propto \chi^{(2)} \int_{-\frac{L}{2}}^{\frac{L}{2}} \mathrm{d}z\, \hat{E}_{\mathrm{p}}^{(+)}(z,t) \hat{E}_{\mathrm{s}}^{(-)}(z,t) \hat{E}_{\mathrm{t}}^{(-)}(z,t) + h.c., \tag{11.13}$$

where p labels the pump, s the signal, and t the trigger field. We further restrict ourselves to collinear propagation along the z-axis of a crystal of length L, neglecting the transverse degrees of freedom. Their impact will be discussed later in this chapter.

The positive and negative frequency parts of the quantum fields in Eq. (11.13) are defined as

$$\hat{E}_{\mathrm{x}}^{(+)} = \hat{E}_{\mathrm{x}}^{(-)\dagger} = A \int \mathrm{d}\omega_{\mathrm{x}} \exp\left[i \left(k_{\mathrm{x}}(\omega_{\mathrm{x}}) z - \omega_{\mathrm{x}} t\right)\right] \hat{a}_{\mathrm{x}}(\omega_{\mathrm{x}}), \tag{11.14}$$

where all constant factors have been merged into the overall constant A and $\hat{a}_{\mathrm{x}}(\omega_{\mathrm{x}})$ is the photon annihilation operator for a monochromatic frequency ω_{x} with propagation constant $k(\omega_{\mathrm{x}})$. The exact nature of the signal and trigger fields is dependent on the applied pump field and the $\chi^{(2)}$-nonlinearity of the crystal. They may be emitted into identical polarizations (type-0/type-I PDC) or into orthogonal polarizations (type-II PDC) [13,14]. Due to the weakness of the nonlinear interaction the incoming pump field must be relatively strong and may be treated as a classical field

$$E_{\mathrm{p}}^{(+)} = E_{\mathrm{p}}^{(-)*} = \int \mathrm{d}\omega_{\mathrm{p}} \alpha(\omega_{\mathrm{p}}) \exp\left[i \left(k_{\mathrm{p}}(\omega_{\mathrm{p}}) z - \omega_{\mathrm{p}} t\right)\right]. \tag{11.15}$$

In Eq. (11.15) the function $\alpha(\omega_{\mathrm{p}})$ describes the spectrum and amplitude of the pump field, which may vary from a delta function $E_{\mathrm{p}}\, \delta(\omega_{\mathrm{p}} - \omega_{\mathrm{c}})$ for cw laser sources with central frequency ω_{c}, to more complex distributions for pulsed laser systems.

We study parametric down-conversion in the Schrödinger picture by calculating the generated state following the presentation in [15]

$$|\psi\rangle_{\mathrm{PDC}} = \exp\left[-\frac{i}{\hbar}\int_{t_0}^{t} \mathrm{d}t'\, \hat{H}_{\mathrm{PDC}}(t')\right]|0\rangle\,. \tag{11.16}$$

We perform a perturbation expansion of Eq. (11.16) to write the PDC process as

$$\begin{aligned}|\psi\rangle_{\mathrm{PDC}}^{(\mathrm{full})} = |0\rangle - \frac{i}{\hbar}\int_{t_0}^{t} \mathrm{d}t'\, \hat{H}_{\mathrm{PDC}}(t')\,|0\rangle \\ + \left(\frac{i}{\hbar}\right)^2 \int_{t_0}^{t} \mathrm{d}t'\, \hat{H}_{\mathrm{PDC}}(t') \int_{t_0}^{t'} \mathrm{d}t''\, \hat{H}_{\mathrm{PDC}}(t'')\,|0\rangle + \cdots,\end{aligned} \tag{11.17}$$

where the zero-order term describes the vacuum emission, the first-order term photon-pair emission, the second-order term four-photon emission, and so on. The emission of higher-order photon pairs can be safely ignored as long as the incoming pump field is not too bright and the probability of multi-pair generation is sufficiently small [16,17]. We hence restrict ourselves to the expansion up to first order

$$|\psi\rangle_{\mathrm{PDC}} \approx |0\rangle - \frac{i}{\hbar}\int_{t_0}^{t} \mathrm{d}t'\, \hat{H}_{\mathrm{PDC}}(t')\,|0\rangle\,, \tag{11.18}$$

which gives us the emitted *not-normalized* two-photon PDC state. Higher-order expansion terms and their effects on the heralding of single photons are discussed in Section 11.2.4.

Combining Eqs. (11.13), (11.14), (11.15), and (11.18), we arrive at

$$\begin{aligned}\int_{t_0}^{t} \mathrm{d}t'\, \hat{H}_{\mathrm{PDC}}(t') = B \int_{t_0}^{t} \mathrm{d}t' \int_{-\frac{L}{2}}^{\frac{L}{2}} \mathrm{d}z \iiint \mathrm{d}\omega_{\mathrm{p}}\mathrm{d}\omega_{\mathrm{s}}\mathrm{d}\omega_{\mathrm{t}}\, \alpha(\omega_{\mathrm{p}}) \\ \times \exp\left[-i\left(\omega_{\mathrm{p}} - \omega_{\mathrm{s}} - \omega_{\mathrm{t}}\right)t'\right] \\ \times \exp\left[i\left(k_{\mathrm{p}}(\omega_{\mathrm{p}}) - k_{\mathrm{s}}(\omega_{\mathrm{s}}) - k_{\mathrm{t}}(\omega_{\mathrm{t}})\right)z\right]\hat{a}_{\mathrm{s}}^{\dagger}(\omega_{\mathrm{s}})\hat{a}_{\mathrm{t}}^{\dagger}(\omega_{\mathrm{t}}) + h.c.,\end{aligned} \tag{11.19}$$

where we merged all constants into an overall factor B. Performing the z-integration we obtain

$$\begin{aligned}\int_{t_0}^{t} \mathrm{d}t\, \hat{H}_{\mathrm{PDC}}(t') = B \int_{t_0}^{t} \mathrm{d}t' \iiint \mathrm{d}\omega_{\mathrm{p}}\mathrm{d}\omega_{\mathrm{s}}\mathrm{d}\omega_{\mathrm{t}}\alpha(\omega_{\mathrm{p}}) \\ \times \exp\left[-i\left(\omega_{\mathrm{p}} - \omega_{\mathrm{s}} - \omega_{\mathrm{t}}\right)t'\right] \\ \times L\,\mathrm{sinc}\left[\left(k_{\mathrm{p}}(\omega_{\mathrm{p}}) - k_{\mathrm{s}}(\omega_{\mathrm{s}}) - k_{\mathrm{t}}(\omega_{\mathrm{t}})\right)\frac{L}{2}\right]\hat{a}_{\mathrm{s}}^{\dagger}(\omega_{\mathrm{s}})\hat{a}_{\mathrm{t}}^{\dagger}(\omega_{\mathrm{t}}) + h.c..\end{aligned} \tag{11.20}$$

Note that the integration was performed from $-\frac{L}{2}$ to $\frac{L}{2}$, which assumes a pump with no extra phase factors in the center of the crystal. A pump pulse with no

additional phase factor at the beginning of the interaction leads to an additional phase factor in the end result.

As a next step we evaluate the time-integration by expanding the bounds to plus and minus infinity. This is justified since we regard the state long before and after the interaction in the crystal. The integration of the time-dependent part then results in a delta function $2\pi\,\delta(\omega_\mathrm{p}-\omega_\mathrm{s}-\omega_\mathrm{t})$, and we subsequently take the integral over the pump frequencies ω_p

$$\int_{-\infty}^{\infty}\mathrm{d}t\;\hat{H}_\mathrm{PDC}(t') = 2\pi\,B\iint \mathrm{d}\omega_\mathrm{s}\,\mathrm{d}\omega_\mathrm{t}\,\alpha(\omega_\mathrm{s}+\omega_\mathrm{t}) \times L\,\mathrm{sinc}\left[\Delta k(\omega_\mathrm{s},\omega_\mathrm{t})\frac{L}{2}\right]\hat{a}_\mathrm{s}^\dagger(\omega_\mathrm{s})\hat{a}_\mathrm{t}^\dagger(\omega_\mathrm{t}) + h.c.. \quad (11.21)$$

Here we have introduced the shorthand $\Delta k(\omega_\mathrm{s},\omega_\mathrm{t}) = k_\mathrm{p}(\omega_\mathrm{s}+\omega_\mathrm{t}) - k_\mathrm{s}(\omega_\mathrm{s}) - k_\mathrm{t}(\omega_\mathrm{t})$. With Eq. (11.21), we are able to write the generated PDC state as

$$\begin{aligned}|\psi\rangle_\mathrm{PDC} &= |0\rangle + B'\iint \mathrm{d}\omega_\mathrm{s}\mathrm{d}\omega_\mathrm{t}\,\alpha(\omega_\mathrm{s}+\omega_\mathrm{t})\mathrm{sinc}\left[\Delta k\left(\omega_\mathrm{s},\omega_\mathrm{t}\right)\frac{L}{2}\right]\hat{a}_\mathrm{s}^\dagger(\omega_\mathrm{s})\hat{a}_\mathrm{t}^\dagger(\omega_\mathrm{t})\,|0\rangle \\ &= |0\rangle + B'\iint \mathrm{d}\omega_\mathrm{s}\mathrm{d}\omega_\mathrm{t}\,\alpha(\omega_\mathrm{s}+\omega_\mathrm{t})\Phi(\omega_\mathrm{s},\omega_\mathrm{t})\hat{a}_\mathrm{s}^\dagger(\omega_\mathrm{s})\hat{a}_\mathrm{t}^\dagger(\omega_\mathrm{t})\,|0\rangle \\ &= |0\rangle + B'\iint \mathrm{d}\omega_\mathrm{s}\mathrm{d}\omega_\mathrm{t}\,f(\omega_\mathrm{s},\omega_\mathrm{t})\hat{a}_\mathrm{s}^\dagger(\omega_\mathrm{s})\hat{a}_\mathrm{t}^\dagger(\omega_\mathrm{t})\,|0\rangle\,, \end{aligned} \quad (11.22)$$

with a scaling factor $B' \propto E_\mathrm{p}L$, which depends linearly on the crystal length L and the field amplitude of the pump field.

As described above, PDC creates two-photon states with a given joint-spectral amplitude (JSA) $f(\omega_\mathrm{s},\omega_\mathrm{t})$. The exact shape of $f(\omega_\mathrm{s},\omega_\mathrm{t})$ is defined by the form of the pump distribution $\alpha(\omega_\mathrm{s}+\omega_\mathrm{t})$, and by the phase-matching function $\Phi(\omega_\mathrm{s},\omega_\mathrm{t})$ determined by the length and the dispersion of the crystal. An example of all three for PDC pumped by a pulsed laser system is presented in Fig. 11.2.

The pump distribution function $\alpha(\omega_\mathrm{s}+\omega_\mathrm{t})$ of Eq. (11.22) reflects the conservation of energy during the process. All pairs created inside satisfy $\omega_\mathrm{p}-\omega_\mathrm{s}-\omega_\mathrm{t}=0$, whereas the phase-matching function $\Phi(\omega_\mathrm{s},\omega_\mathrm{t})$ depicts

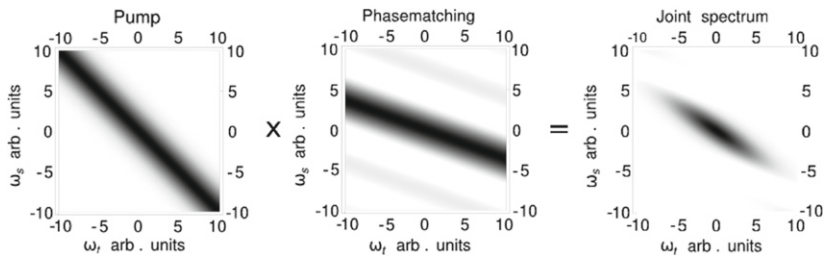

FIGURE 11.2 Exemplary pump spectrum $\alpha(\omega_\mathrm{s}+\omega_\mathrm{t})$, phase-matching function $\Phi(\omega_\mathrm{s},\omega_\mathrm{t})$, and joint-spectral amplitude distribution $f(\omega_\mathrm{s},\omega_\mathrm{t})$ of a PDC state.

momentum conservation $k_p(\omega_p) - k_s(\omega_s) - k_t(\omega_t) = 0$. Taken together these functions form the joint-spectral-amplitude distribution of the created photon pairs satisfying both energy and momentum conservation.

11.2.3 Heralding Single Photons from PDC

If the two photons generated by PDC can be efficiently and deterministically separated, for example distinguishing them by their polarizations or their wavelengths, then the detection of one photon heralds the generation of the other. Therefore we have to detect the trigger photon in order to signal the presence of its partner—the signal—from the PDC state in Eq. (11.22). A single-photon avalanche diode (SPAD) with detection efficiency η can be described by the "click" or trigger detection observable $\hat{\pi}_1$ and "no-click" or no detection observable $\hat{\pi}_0$ (see Chapters 2 and 4)

$$\begin{aligned}\hat{\pi}_0 &= \int \mathrm{d}\omega \; |0,\omega\rangle \langle 0,\omega| \,, \\ \hat{\pi}_1 &= \int \mathrm{d}\omega \, \eta \, |1,\omega\rangle \langle 1,\omega| \,, \end{aligned} \tag{11.23}$$

where $|0,\omega\rangle$ implies vacuum at frequency ω and $|1,\omega\rangle$ a single photon at the same frequency. Since we restrict ourselves to single photons arriving at the detector, higher-photon-number components in $\hat{\pi}_0$ and $\hat{\pi}_1$ are omitted. These SPAD detectors are also known as binary detectors, since they are not able to distinguish the number of photons arriving simultaneously.

The probability of detecting the trigger photon and successfully heralding a single-photon state is directly related to the efficiency of the detector η and the amplitude of the two-photon state created in the down-conversion process B'. While employing efficient detectors is a straightforward method to boost the heralding efficiency, care has to be taken when engineering the PDC process. It might seem straightforward to increase the pump intensity in order to boost the amplitude of the two-photon component in the PDC state. One should however note that at some point the perturbation expansion performed in Eq. (11.18) breaks down and higher-order components have to be considered to correctly model the process.

Using Eqs. (11.22) and (11.23) we calculate the *not-normalized* heralded single-photon state after a successful detection event

$$\begin{aligned}\rho_s &= \mathrm{tr}\left(\pi_1 \, |\psi\rangle \langle\psi|\right) \\ &= \int \mathrm{d}\omega_t'' \, \langle \omega_t''| \left[\eta \iint \mathrm{d}\omega_s \omega_t \, f(\omega_s,\omega_t) \iint \mathrm{d}\omega_s' \omega_t' f^*(\omega_s',\omega_t') \, |\omega_s,\omega_t\rangle \langle \omega_s',\omega_t'| \right] |\omega_t''\rangle \\ &= \eta \iint \mathrm{d}\omega_s \, \mathrm{d}\omega_s' \left[\int \mathrm{d}\omega_t'' \, f(\omega_s,\omega_t'') \, f^*(\omega_s',\omega_t'') \right] |\omega_s\rangle \langle \omega_s'| \\ &= \eta \iint \mathrm{d}\omega_s \, \mathrm{d}\omega_s' \, j(\omega_s,\omega_s') \, |\omega_s\rangle \langle \omega_s'| \,. \end{aligned} \tag{11.24}$$

Equation (11.24) accurately describes the heralded single-photon state with density matrix $j(\omega_s,\omega_s')$ that is determined by joint-spectral amplitude $f(\omega_s,\omega_t)$ of the PDC state. $j(\omega_s,\omega_s')$ already provides some intuition about the purity of the state. If $j(\omega_s,\omega_s')$ has circular symmetry, and is therefore separable, it can be written as $j(\omega_s,\omega_s') = f(\omega_s)f^*(\omega_s')$ and the photon is heralded in a pure state

$$\begin{aligned}\rho_s &= \eta^2 \iint \mathrm{d}\omega_s\, \mathrm{d}\omega_s' f(\omega_s) f^*(\omega_s') \left|\omega_s\right\rangle \left\langle\omega_s'\right| \\ &= \eta^2 \int \mathrm{d}\omega_s f(\omega_s) \left|\omega_s\right\rangle \int \mathrm{d}\omega_s' f^*(\omega_s') \left\langle\omega_s'\right| = \left|\psi_s\right\rangle \left\langle\psi_s\right|, \end{aligned} \tag{11.25}$$

because pure states always correspond to circular-shaped $j(\omega_s,\omega_s')$ [18,19].

To obtain further insight into the PDC process we use the Schmidt decomposition theorem [20]. It states that every well-behaved *normalized* two-dimensional function can be decomposed as a sum over a range of positive values κ_k and complete sets of orthonormal functions $g_k(x)$ and $h_k(x)$

$$f(x,y) = \sum_k \kappa_k g(x) h(y), \tag{11.26}$$

with $\sum_k \kappa_k^2 = 1$. Using this decomposition we rewrite the PDC state in Eq. (11.22) as

$$\left|\psi\right\rangle_{\mathrm{PDC}} = \left|0\right\rangle + b \iint \mathrm{d}\omega_s \mathrm{d}\omega_t \sum_k \kappa_k g_k(\omega_s) h_k(\omega_t) \hat{a}_s^\dagger(\omega_s) \hat{a}_t^\dagger(\omega_t) \left|0\right\rangle, \tag{11.27}$$

where b is used to normalize $B' f(\omega_s,\omega_t)$. Carrying out a basis transformation from the single-frequency modes $\hat{a}_s^\dagger(\omega_s)$ and $\hat{a}_t^\dagger(\omega_t)$ to the broadband frequency modes $\hat{A}_k^\dagger$ and $\hat{B}_k^\dagger$ [21], defined as

$$\begin{aligned}\hat{A}_k^\dagger &= \int \mathrm{d}\omega_s\, g_k(\omega_s) \hat{a}_s^\dagger(\omega_s), \\ \hat{B}_k^\dagger &= \int \mathrm{d}\omega_t\, h_k(\omega_t) \hat{a}_t^\dagger(\omega_t), \end{aligned} \tag{11.28}$$

the PDC state takes the form of a sum over the broadband modes $\hat{A}_k^\dagger$ and $\hat{B}_k^\dagger$

$$\left|\psi\right\rangle_{\mathrm{PDC}} = \left|0\right\rangle + b \sum_k \kappa_k \hat{A}_k^\dagger \hat{B}_k^\dagger \left|0\right\rangle. \tag{11.29}$$

Hence the photon pair generated during the PDC process with a given frequency distribution $f(\omega_s,\omega_t)$ is emitted into a superposition of strictly correlated broadband frequency modes $\hat{A}_k^\dagger$ and $\hat{B}_k^\dagger$. If one photon is detected in mode $\hat{B}_k^\dagger$ its partner is present in mode $\hat{A}_k^\dagger$, and vice versa.

In a similar manner we expand the detection observables $\hat{\pi}_0$ and $\hat{\pi}_1$ from Eq. (11.23) in the broadband basis of the trigger modes

$$\hat{\pi}_0 = \sum_{\mathrm{k}} |0, h_{\mathrm{k}}(\omega_{\mathrm{t}})\rangle \langle 0, h_{\mathrm{k}}(\omega_{\mathrm{t}})| ,$$
$$\hat{\pi}_1 = \sum_{\mathrm{k}} \eta\, |1, h_{\mathrm{k}}(\omega_{\mathrm{t}})\rangle \langle 1, h_{\mathrm{k}}(\omega_{\mathrm{t}})| . \tag{11.30}$$

In this broadband formalism, using Eqs. (11.29) and (11.30) the density operator of the heralded single photon can be represented as

$$\rho_{\mathrm{s}} = \sum_{\mathrm{k}} \kappa_{\mathrm{k}}^2\, |1, g(\omega_{\mathrm{s}})\rangle \langle 1, g(\omega_{\mathrm{s}})| . \tag{11.31}$$

Hence after the detection process the heralded single photon is projected into a statistical mixture of broadband single-photon states with probabilities κ_{k}^2. The number of κ_{k} and their respective amplitudes depend on the joint spectrum of the initial PDC state. The reason for this behavior can be attributed to the single-photon detector, which cannot distinguish between the different optical modes. It is impossible to know, in principle, which optical mode was responsible for triggering the detection event. Therefore the heralded single photon is emitted into a statistical mixture of broadband modes.

There exist a variety of different measures to characterize the purity of the heralded single photons. Common are the cooperativity $K = \frac{1}{\sum_{\mathrm{k}} \kappa_{\mathrm{k}}^4}$ [22], which is unity if the signal photon is in a pure state and increases with increased amounts of mixing, or the von Neumann entropy $S = -\sum_{\mathrm{k}} \kappa_{\mathrm{k}}^2 \log_2 \kappa_{\mathrm{k}}^2$ [23], which ranges from zero for a pure signal photon to infinity for rising degrees of impurity.

11.2.4 Heralding Pure Single-Photon Fock States

We now turn our attention to the heralding of pure single photons, or single-photon Fock states, which are vital for various quantum information applications, especially quantum computing. While the heralded signal photons from the PDC process can be delivered in a good approximation of a single-photon state for suitable experimental parameters, the state is not necessarily pure. In order to achieve a pure single-photon state various methods can be pursued.

11.2.4.1 Spectral Purity: Filtering

The simplest and most straightforward approach to create pure Fock states from PDC uses narrowband spectral filtering in the heralding arm [24]. The spectral filter acts as a beamsplitter through which only a single frequency is transmitted

to the detector and all other frequencies are reflected or absorbed by the filter. The general input-output relation of the filter can be written as

$$\hat{a}(\omega) \Rightarrow T(\omega)\hat{a}(\omega) + R(\omega)\hat{b}(\omega), \tag{11.32}$$

where $T(\omega)$ and $R(\omega)$ obey the standard beamsplitter relations. If we assume a delta-function-like transmission of the filter at frequency ω_f, i.e., $T(\omega) = \delta(\omega - \omega_\mathrm{f})$ and condition on the heralding photon passing the filter, the PDC state becomes

$$\begin{aligned} |\psi\rangle_\mathrm{PDC} &= \iint \mathrm{d}\omega_\mathrm{s} d\omega_\mathrm{t} f(\omega_\mathrm{s},\omega_\mathrm{t})\delta(\omega_\mathrm{f} - \omega_\mathrm{t})\hat{a}_\mathrm{s}^\dagger(\omega_\mathrm{s})\hat{a}_\mathrm{t}^\dagger(\omega_\mathrm{t})\,|0\rangle \\ &= \int \mathrm{d}\omega_\mathrm{s} f(\omega_\mathrm{s},\omega_\mathrm{f})\hat{a}_\mathrm{s}^\dagger(\omega_\mathrm{s})\hat{a}_\mathrm{t}^\dagger(\omega_\mathrm{f})\,|0\rangle\,. \end{aligned} \tag{11.33}$$

After detection of the filtered trigger the heralded signal photon is projected onto the *not*-normalized signal state

$$|\psi\rangle_\mathrm{s} = \eta \int \mathrm{d}\omega_\mathrm{s} f(\omega_\mathrm{s},\omega_\mathrm{f})\hat{a}_\mathrm{s}^\dagger(\omega_\mathrm{s})\,|0\rangle\,. \tag{11.34}$$

The heralded signal is in a *pure* single-photon state, yet still spans a range of different frequencies, i.e., it is in a broadband single-mode quantum state. Hence the multimode nature of the PDC state is effectively suppressed by filtering the trigger photon down to a single-frequency mode. This is due to the fact that, after the filtering, only a *single* optical frequency mode is impinging on the detector, which leads to a "collapse" of the signal photon into pure, but broadband, single-photon Fock state. However, in practice, care has to be taken when performing the filtering because the filter bandwidth will always have some finite width. This limits the purity of the heralded single-photon state. Additionally standard filters do not feature unit transmissivity. Thus, in this approach to producing pure single-photon states the majority of the trigger photons are absorbed by the filter, severely reducing the rate of successful heralding events. In addition, the losses associated with filtering the trigger may enhance the multi-photon contribution of the PDC state to the heralded signal [25].

11.2.4.2 Spectral Purity: Extended Phase Matching and Group-Velocity Matching

A more sophisticated approach to herald Fock states is to engineer the down-conversion process itself. If the generated PDC state is emitted into only a single-frequency mode, such as $|\psi\rangle_\mathrm{PDC} = |0\rangle + \hat{A}^\dagger\hat{B}^\dagger\,|0\rangle$, then the heralded single photon will be projected into the pure state $\rho_\mathrm{s} = \hat{A}^\dagger\,|0\rangle\,\langle 0|\,\hat{A}$.

This configuration can be achieved if the shape of the joint-spectral distribution $f(\omega_\mathrm{s},\omega_\mathrm{t})$ is engineered appropriately. The Schmidt decomposition

theorems (Eq. (11.26)) tell us that to obtain a photon pair in a single optical mode, it is necessary for the joint-spectral distribution $f(\omega_s,\omega_t)$ to be factorable as $f(\omega_s,\omega_t) = g(\omega_s)h(\omega_t)$. In other words all κ_k coefficients have to be zero except one. Hence it is necessary to find experimental conditions such that the joint-spectral amplitude distribution from Eq. (11.22)

$$f(\omega_s,\omega_t) = \alpha(\omega_s + \omega_t)\Phi(\omega_s,\omega_t), \tag{11.35}$$

does not feature any frequency correlations between the signal and the trigger.

Consider using a cw pump laser with central frequency ω_c, in which case $f(\omega_s,\omega_t)$ becomes

$$f(\omega_s,\omega_t) = E_p\delta(\omega_s + \omega_t - \omega_c)\Phi(\omega_s,\omega_t). \tag{11.36}$$

In this specific case, the joint-spectral-amplitude distribution is diagonal and continuous in the frequency space (ω_s,ω_t) and hence is not factorable and cannot be written in product form. In fact it is impossible to directly create photon pairs in a single-frequency mode when using a cw laser. Pulsed lasers, however, can achieve the desired effect. Standard pulsed lasers can produce Gaussian-shaped pulses with a given spectral width σ_p and central frequency ω_c, resulting in a JSA is given by

$$\begin{aligned} f(\omega_s,\omega_t) &= A_p \exp\left[-\left(\frac{(\omega_s + \omega_t - \omega_c)^2}{2\sigma_p^2}\right)\right]\Phi(\omega_s,\omega_t) \\ &= A_p \exp\left[-\left(\frac{(\omega_s + \omega_t - \omega_c)^2}{2\sigma_p^2}\right)\right]\operatorname{sinc}\left[\Delta k(\omega_s,\omega_t)L/2\right]. \end{aligned} \tag{11.37}$$

From Eq. (11.37) an analytical expression for the factorability condition can be derived (see [26])

$$\frac{2}{\sigma^2} + \gamma L^2\left(\frac{1}{v_p} - \frac{1}{v_s}\right)\left(\frac{1}{v_p} - \frac{1}{v_t}\right) = 0, \tag{11.38}$$

where v_i labels the group-velocities of the three interacting fields and $\gamma \approx 0.193$. Therefore the condition for directly generating PDC states that will lead to the heralding of pure single-photon Fock states is to find a crystal in which the pump travels slower than the trigger wave, and travels faster than the signal wave (or vice versa). Engineering the source in this manner has the advantage that no filtering is required, and hence the generated trigger photons arrive at the detector with low loss, resulting in high heralding rates. It is indeed possible to find materials that can fulfill these conditions by generating these waves in different polarizations [26] or directions [27]. Examples will be discussed in the remainder of this section.

11.2.4.3 Photon-Number Purity

Based on the quantum state produced from PDC, we must consider the details of the photon-number distribution of the heralded single-photon states achieved by detecting one mode from a photon pair. Given the strict photon-pair correlations imposed by the PDC process there will be multi-photon terms from the higher-order emissions, however, if the heralding is done by a perfect single-photon detector with ideal coupling efficiency, this scheme would allow to herald perfect single photons.

The photon-number statistics can be derived for the state generated by PDC by applying the PDC Hamiltonian in the approximation of a strong pump mode, acting on two optical modes a_1,a_2 in the form $H_{\mathrm{PDC}} = \varepsilon(a_1^\dagger a_2^\dagger + a_1 a_2)$, where ε is an interaction parameter that includes the nonlinearity, the phase-matching, and the interaction time. The state, including the higher-order photon-number terms with their correct amplitudes, can be estimated by evolution of this Hamiltonian for vacuum inputs

$$\exp\left(-i\,H_{\mathrm{PDC}}\right)|0,0\rangle_{\mathrm{a_1,a_2}}. \tag{11.39}$$

For $\varepsilon < 1$ this yields the output state in the form

$$|\Psi\rangle_{\mathrm{PDC}} = c_0|00\rangle_{\mathrm{a_1,a_2}} + c_1|11\rangle_{\mathrm{a_1,a_2}} + c_2|22\rangle_{\mathrm{a_1,a_2}} + \cdots, \tag{11.40}$$

with the amplitudes $c_{\mathrm{i}} = \sqrt{1-\varepsilon^2}\cdot\varepsilon^i$ [28]. One of the modes will be the trigger mode, the other the signal. Because the detection process on the trigger photon corresponds, at least in principle, to a photon-number measurement, the remaining photon is no longer in a superposition of number states, as originally given by the PDC. Rather it is a mixture of number states weighted with the appropriate probability. Typically the purity in photon numbers for the heralded single-photon state is characterized by the normalized second-order correlation function $g^{(2)}(t_1,t_2)$, see Chapter 2: Photon statistics and measurements.

The residual photon statistics of the heralded photon will depend on the efficiency of the trigger detection, and on the type of trigger detector, specifically whether it is a click/no-click detector (often referred to as a threshold detector); or a photon-number resolving detector. See Chapters 3–7 for further details on single-photon detectors.

As discussed earlier in this book, the response of a click/no-click detector with single-photon detection efficiency η to two or more photons is given by the combined probability that any number of the incident photons produces a click. For example, with two photons impinging on the detector, $|2\rangle\langle 2|$, a click-event may be generated with probability η^2 in the case that both photons are absorbed, or with probability $\eta(1-\eta)$, that one is absorbed and not the other. Because the latter combination can occur in two different ways, the combined probability for a "click" is $\eta^2 + 2\eta(1-\eta) = 1 - (1-\eta)^2$. Generalizing this approach leads to the click probabilities for a given n-Fock state $P_{\mathrm{BD}}(n) = 1 - (1-\eta)^{(n)}$, with measurement operator

$\hat{\Pi}_{\text{“click”}} = \sum_{\text{n}} \left(1 - (1-\eta)^n\right) |n\rangle \langle n|$ (see Chapter 9, and the models described in [29,30]). A photon-number resolving (PNR) detector has a different characteristic, as it can discriminate the number of photons that are detected. For instance, the measurement operator for the detection of exactly one photon has the form $\hat{\Pi}_1 = \sum_{\text{N}=1}^{\infty} \binom{N}{1} \left(1-\eta\right)^{N-1} \eta \, |N\rangle \langle N|$, see Refs. [31,30].

In order to determine the photon-number state of the heralded output, these photon-number detection characteristics are used to describe the trigger detector receiving the multi-photon state generated from PDC, shown in Eq. (11.40). For a click/no-click detector this gives a heralded state described by the density matrix:

$$\rho_{\text{heralded1}} = \frac{1}{M} Tr_{\text{a1}} (\hat{\Pi}_{\text{PDC}} |\psi\rangle \langle\psi|_{\text{PDC}}) \tag{11.41}$$

$$= Q|0\rangle\langle 0|_{\text{a}_2} + P_1|C_1|^2|1\rangle\langle 1|_{\text{a}_2} + P_2|C_2|^2|2\rangle\langle 2|_{\text{a}_2} + \cdots, \tag{11.42}$$

which describes a mixture of photon-number states, where $P_1, P_2, \ldots$ are the detection probabilities for a “click” in the trigger detector, as defined above for the respective photon-number terms, $C_1, C_2, \ldots$ are the amplitudes of the terms from the PDC state, Q is the probability that the trigger detector does not fire, and $\frac{1}{M}$ is the renormalization factor.

The simulation in Fig. 11.3 shows how $g^{(2)}(0)$ changes with the probability of detecting a trigger photon within the time unit of the system (for example this could be the duration of the pump pulse or the timing window of the detectors), under variation of the interaction strength of the PDC. Essentially this result shows that with a higher pair production through stronger pumping, the photon-number purity suffers severely. One must therefore choose the PDC interaction strength according to what can be tolerated in the specific application [114].

11.2.4.4 Improving the Heralding Rates with Switched PDC

Given the non-deterministic behavior of the PDC interaction, the heralding of a single-photon state will only occur with a low probability. As shown above, the pump strength cannot be increased arbitrarily, because as the probabilities for a trigger detection increase, so will the likelihood of multi-pair emission.

One elegant solution is to combine multiple PDC sources using an array of switches so that the signal output of a PDC source from which a trigger photon was successfully detected can be switched into a single combined output. If enough PDC sources are combined, the chances that at least one PDC process triggers is close to 1, but at the same time each individual heralded photon can be produced with the desired low $g^{(2)}(0)$.

Several possible schemes of this type have been studied, including parallel switches for several spatial modes [32], and switched photon storage in rings or cavities [33]. Generally, all these schemes are challenging to implement, because the additional optical losses caused by currently available switching

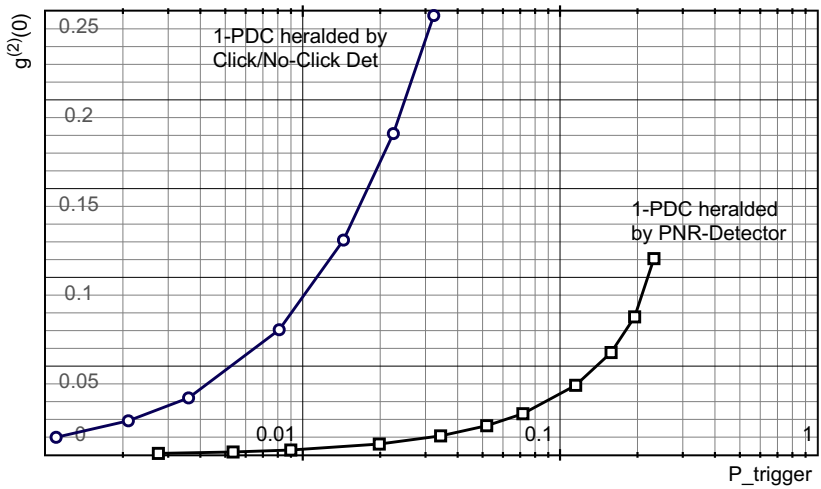

FIGURE 11.3 Single-photon quality $g^{(2)}(0)$ for photons heralded from PDC, versus the probability for a click in the trigger detector. The pump strength of the PDC is varied in the simulation. The assumed detector efficiencies are 65% for the click/no-click detector and 95% for the PNR detector.

technologies outweigh the gains from the combination of several PDC's, as was analyzed in [34].

11.3 BULK-CRYSTAL PDC

In this section we explore parametric down-conversion in *bulk* crystals, i.e., standard nonlinear crystals without poling or embedded waveguides. The vast majority of PDC sources have been realized in bulk crystals, and while they are increasingly being supplanted by periodically-poled structures in continuous-wave down-conversion—due to the higher achievable brightnesses—they are still the system of choice for the generation of multi-photon states in pulsed-pump PDC.

11.3.1 Birefringent Phase-Matching

In Section 11.2.2, we derived the general PDC Hamiltonian. To generate PDC in practice, the three interacting fields have to conserve energy, i.e., the frequencies match

$$\omega_{\mathrm{p}} = \omega_{\mathrm{s}} + \omega_{\mathrm{t}}, \tag{11.43}$$

and conserve momentum *in the crystal*, i.e., the phases match

$$\mathbf{k}_{\mathrm{p}} = \mathbf{k}_{\mathrm{s}} + \mathbf{k}_{\mathrm{t}}, \tag{11.44}$$

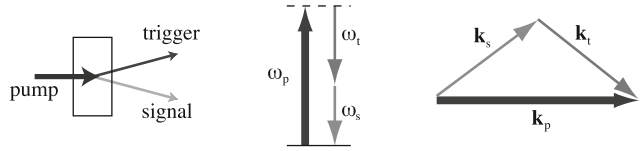

FIGURE 11.4 Energy and momentum conversion between a pump (p), a signal (s), and a trigger field (t) in parametric down-conservation.

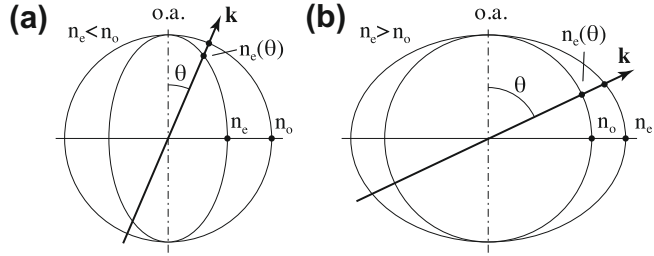

FIGURE 11.5 Refractive index for a light field **k** propagating in birefringent crystals. (a) Negative uniaxial crystal with $n_o > n_e$. (b) Positive uniaxial crystal with $n_e > n_o$. o.a.: optical axis.

as shown schematically in Fig. 11.4. The phase-matching condition Eq. (11.44) is subject to dispersion in the nonlinear medium, through $k = \omega n(\omega)/c$, see also Eq. (11.7). To satisfy Eq. (11.44), the polarizations and wave vectors of the interacting fields must be carefully chosen such that $\omega_p n_p(\omega_p) = \omega_s n_s(\omega_s) + \omega_t n_t(\omega_t)$. In an isotropic bulk crystal however, the normal dispersion ensures that this is not possible while also fulfilling Eq. (11.43).

The solution is to use anisotropic materials, in which fields with different polarizations experience different refractive indices. The plane containing the optical axis and the pump wave vector is called the principal plane, and we denote a light beam polarized orthogonally to that plane the *ordinary* (o) and the beam polarized within that plane the *extraordinary* (e) beam. As can be seen in Fig. 11.5 for a uniaxial crystal, the refractive index for the ordinary beam, n_o, is independent of the field orientation in the crystal. The extraordinary refractive index, shown as an ellipsoid, is dependent on the angle θ between the field vector and the optical axis of the crystal, $n_e(\theta) = (\cos^2(\theta)/n_o^2 + \sin^2(\theta)/n_e^2)^{-1/2}$.

Phase-matching in such a material can be achieved for orthogonally-polarized fields through birefringent phase-matching, which is most commonly done by tuning the angle between the crystal axes and the interacting fields. This technique is also called *critical* phase-matching, because it is quite sensitive to deviations from optimal conditions and thus limits the angular, spectral, and temperature acceptance bandwidth.

Alternatively, the angle θ can be set to 90° and the phase-matching can be achieved by varying the temperature of the crystal, which changes the relative

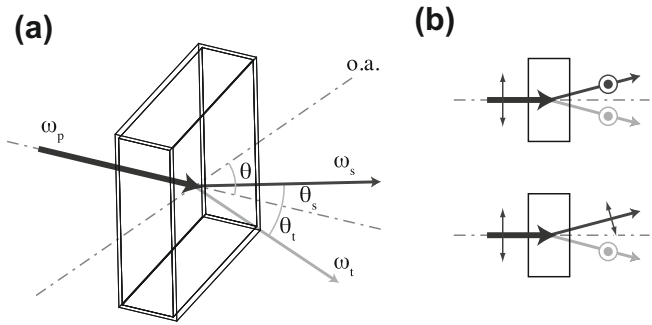

FIGURE 11.6 Parametric down-conversion in a bulk crystal. (a) Angular phase matching. The optical crystal axis (o.a.) spans an angle θ with the pump field. The down-converted fields emerge at angles θ_s and θ_t. (b) PDC in birefringent materials can be achieved via type-I (top) or type-II (bottom) phase matching.

size of the ordinary and extraordinary ellipsoids, Fig. 11.5. This technique is called *non-critical* phase-matching (and sometimes temperature- or 90° phase-matching).

Angular phase matching is schematically shown in Fig. 11.6a. The pump field spans the angles θ_s and θ_t with the two down-converted fields. There are two phase-matching options in this case, type-I down-conversion of a pump beam orthogonally polarized to the two co-polarized down-conversion fields, or type-II down-conversion, where the down-converted fields are orthogonally polarized, see Fig. 11.6b. In a negative uniaxial crystal, type-I phase matching is possible for an extraordinary pump splitting into two ordinary PDC photons, $e \rightarrow o + o$, while type-II PDC can be achieved for $e \rightarrow o + e$. In a positive uniaxial crystal, this situation is inverted, $o \rightarrow e + e$, $o \rightarrow e + o$. The third option, type-0 phase matching where all fields are co-polarized, cannot generally be implemented in bulk materials but is often used in periodically-poled crystals.

One of the challenges of building PDC sources using angle phase-matching is transversal walkoff between the e and o fields. This walkoff restricts the useful length of a bulk crystal and thus limits the photon-pair yield. This can only be avoided by choosing a collinear PDC configuration along one of the crystal axes, which can be achieved by using non-critical phase matching in bulk crystals.

The dispersion relations, i.e., the exact wavelength- and temperature-dependence of the refractive indices, are usually available in the form of empirical *Sellmeier* equations (see [35] for one of the most comprehensive compilations of nonlinear crystal properties). Using these equations, the phase-matching conditions can be solved numerically for a set of target frequencies—which are usually subject to availability of suitable pump lasers and photon detectors. A particularly useful free software suite for this purpose is *SNLO*, written by A. Smith [36]. It contains data for more than 50 commonly used

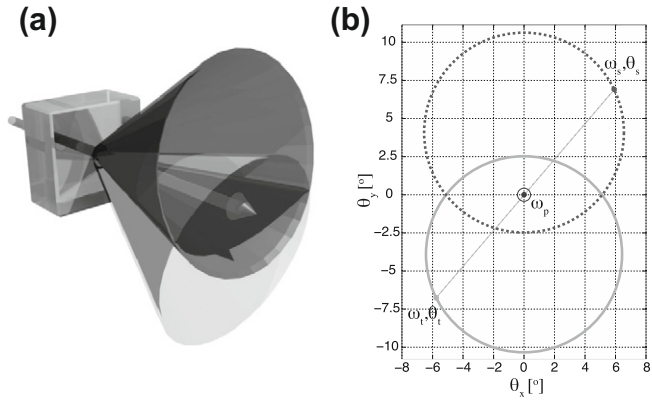

FIGURE 11.7 Non-collinear type-II down-conversion in a BBO crystal, with its optical axis oriented at $\theta = 41°$, pumped at 410 nm.

crystals and allows modeling of most nonlinear optical applications, such as optical parametric oscillators, second-harmonic generation, and parametric down-conversion.

We now present two example solutions for widely used PDC applications. The first is type-II noncollinear PDC in a negative uniaxial β-barium borate (BBO) crystal pumped by a 410 nm laser to generate frequency-degenerate down-conversion at 820 nm. The characteristic emission cones are shown in Fig. 11.7. This geometry is a popular choice for generating polarization-entangled photons, and has had enormous success in experimental quantum information processing since its first demonstration in [8].

The second example is collinear PDC ($\theta_s = \theta_t = 0$) in a biaxial bismuth borate (BiBO) crystal. The BiBO crystal is increasingly replacing BBO due to its higher nonlinearity, as for example demonstrated in [37]. While it is more complicated to calculate phase-matching conditions for biaxial crystals, they are also more versatile. Exemplary tuning curves, for the same pump wavelength of 410 nm, are shown as a function of θ for type-I and type-II phase matching in Fig. 11.8a and b, respectively. These tuning curves show a characteristic difference between type-I and type-II schemes. For frequency-degenerate schemes, where $\omega_s = \omega_t$, the bandwidth of type-I schemes is far broader for a given acceptance angle then for type-II schemes. The bandwidth quickly decreases for type-I as one moves away from degeneracy, whereas it is more or less constant over a wide frequency range for type-II configurations. Furthermore, the type-I configuration does not have a phase-matching solution for angles above the critical angle. A rigorous analysis of non-collinear type-II PDC in BiBO has recently been conducted [38].

Once a crystal has been chosen and a phase-matching solution has been found, the next design challenges are: to optimise (i) the PDC brightness, (ii) the photon heralding efficiency, and (iii) the heralded-photon purity. As we shall

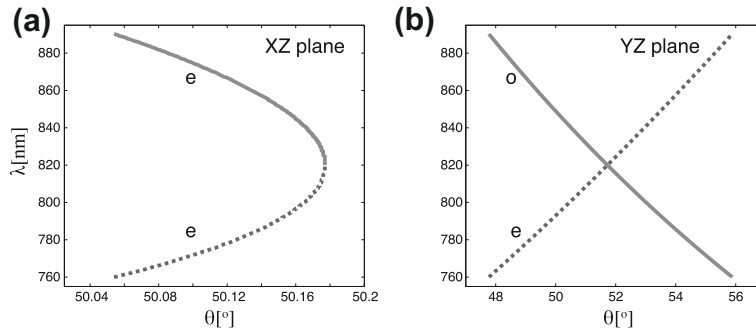

FIGURE 11.8 Tuning curves for PDC in a biaxial BiBO crystal, as a function of optical axis orientation θ, pumped at 410 nm. (a) Type-I phase-matching, $o \rightarrow e + e$, with the crystal cut along the X-Z plane. (b) Type-II phase-matching, $e \rightarrow o + e$, along the Y-Z plane.

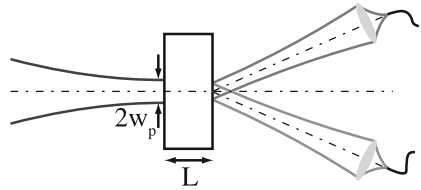

FIGURE 11.9 Fiber coupling non-collinear down-conversion light. The pump beam is focused to a waist size w_p in the crystal of length L. The PDC modes are coupled into two optical fibers, whose mode field diameter is matched to the PDC mode with two lenses.

see, these are intimately interconnected. The source brightness can be defined as either the collected or detected number of photon pairs per unit time and unit pump power. Depending on the application, this is sometimes further divided by the PDC output bandwidth, giving the spectral brightness. Typical values are summarized in Fig. 11.32.

The heralding efficiency is the probability of a PDC photon being in the signal mode conditioned on detection of the trigger photon (see also the formal definition in Section 11.2.3). Both the brightness and the heralding efficiency are primarily controlled by optical mode-matching of the pump and PDC fields, see Fig. 11.9. Early experiments relied mostly on pinholes for spatial filtering and collection of the PDC light, a technique that was soon replaced by the use of single-mode. One early analysis showed that fibre coupling can be optimized for a given spectral range by tuning the (continuous-wave) pump-beam focusing to match the angular spread of the PDC emission to the angular acceptance width of the fibre modes [39]. This work was followed by more sophisticated numerical models for both the continuous-wave [40,41] and—for heralding applications—the pulsed-pump cases [42]. Due to the complicated spatio-temporal form of the two-photon state generated in non-collinear PDC, the calculations must be solved numerically. In the following we briefly outline how this problem can be approached [42].

11.3.1.1 Transverse Two-Photon State in Bulk Crystals

In contrast to the derivation of the collinear case in Section 11.2.2, the exact description of non-collinear PDC includes the transverse components of the interacting fields. The positive and negative components of the field operators (cf. Eq. (11.14)) thus take the form $\hat{E}_{\mathrm{i}}^{(+)}(\mathbf{r}) = \hat{E}_{\mathrm{i}}^{(-)\dagger}(\mathbf{r}) = A \int \mathrm{d}^2\mathbf{k}_{\mathrm{i}} \mathrm{d}\omega_{\mathrm{i}}$ $e^{i\left(\mathbf{k}_{\mathrm{i}}(\omega_{\mathrm{i}})\mathbf{r}-\omega_{\mathrm{i}}t\right)} \hat{a}_{\mathrm{i}}(\mathbf{k}_{\mathrm{i}},\omega_{\mathrm{i}})$. The corresponding two-photon state is

$$|\psi\rangle = \int d^2\mathbf{k}_{\mathrm{s}\perp} d^2\mathbf{k}_{\mathrm{t}\perp} d\omega_{\mathrm{s}} d\omega_{\mathrm{t}} \Phi(\mathbf{k}_{\mathrm{s}\perp},\omega_{\mathrm{s}},\mathbf{k}_{\mathrm{t}\perp},\omega_{\mathrm{t}}) a_{\mathrm{s}}^{\dagger}(\mathbf{k}_{\mathrm{s}\perp},\omega_{\mathrm{s}}) a_{\mathrm{t}}^{\dagger}(\mathbf{k}_{\mathrm{t}\perp},\omega_{\mathrm{t}})|0\rangle, \tag{11.45}$$

with the two-photon amplitude

$$\Phi(\mathbf{k}_{\mathrm{s}\perp},\omega_{\mathrm{s}},\mathbf{k}_{\mathrm{t}\perp},\omega_{\mathrm{t}}) = \int_0^L \mathrm{d}z A_{\mathrm{p}}(\mathbf{k}_{\mathrm{s}\perp} + \mathbf{k}_{\mathrm{t}\perp},\omega_{\mathrm{s}} + \omega_{\mathrm{t}}) e^{i\Delta k_z(\mathbf{k}_{\mathrm{s}\perp}+\mathbf{k}_{\mathrm{t}\perp},\omega_{\mathrm{s}}+\omega_{\mathrm{t}})z}, \tag{11.46}$$

where A_{p} represents the pump field. The phase-mismatch Δk_z is now defined through the z components of the wave vectors involved

$$\begin{aligned}\Delta k_z(\mathbf{k}_{\mathrm{s}\perp}+\mathbf{k}_{\mathrm{t}\perp},\omega_{\mathrm{s}}+\omega_{\mathrm{t}}) = k_{\mathrm{p}z}(\mathbf{k}_{\mathrm{s}\perp}+\mathbf{k}_{\mathrm{t}\perp},\omega_{\mathrm{s}}+\omega_{\mathrm{t}}) \\ - k_{\mathrm{s}z}(\mathbf{k}_{\mathrm{s}\perp},\omega_{\mathrm{s}}) - k_{\mathrm{t}z}(\mathbf{k}_{\mathrm{t}\perp},\omega_{\mathrm{t}}).\end{aligned} \tag{11.47}$$

Equation (11.46) describes the PDC field for all possible output directions, but will only have non-zero amplitude for the propagation directions allowed by the phase-matching conditions. Using these equations one can now tackle the problem of optimizing the key performance parameters of a non-collinear PDC source, for example, by numerically maximizing the overlap of the output wave function with optical fiber modes, as shown in [42]. This treatment also provides a starting point for obtaining conditions for which the joint-spectral PDC amplitude is factorizable, which is the prerequisite for a high heralded-photon purity [115].

11.3.2 Heralded Single Photons from Triggered PDC

A plethora of PDC sources have been demonstrated for the generation of one or more (entangled) photon pairs for experiments in quantum information processing. All of them serve as examples of the creation of heralded single photons via PDC even though they were usually not employed for that purpose.

The creation of *pure* heralded single photons (see theory in Section 11.2.4) via PDC has only recently attracted the focus of in-depth research. In the following we describe two approaches toward this goal. The first investigates how vectorial matching can be used to create pure photons. The second, which can be combined with most other techniques, involves multiplexing downconverters to increase the likelihood of the creation of single pairs while reducing multi-pair emissions.

11.3.2.1 Photon-State Tuning Through Vectorial Matching

In Section 11.2.3 we discussed the theory and necessity of creating photon pairs with a separable joint-spectral amplitude, defined in Eq. (11.35). The goal is to tailor the JSA such that the measurement of the heralding photon does not interfere with the state of the signal photon. In particular, the two photons must not be correlated in frequency. This can be achieved through *group-velocity matching* [26] in one of the following two ways.

Asymmetric JSA

The first is to match the group-velocity of either down-conversion photon to that of the pump field, e.g., $v_t' = v_p'$. This creates a vertical phase-matching function and, consequently, a separable, asymmetric JSA, see Fig. 11.10, which corresponds to emission of one narrowband and one broadband photon. In a bulk crystal, this can be achieved through careful vectorial matching in combination with the proper choice of the spectral properties of the pump laser. However, the necessity of simultaneous phase-matching and group-velocity matching imposes very stringent conditions and can only be achieved for very specific sets of wavelengths in a limited number of nonlinear crystals. This limitation is alleviated by the advent of periodically-poled crystals, which offer more experimental degrees of freedom, as discussed in Section 11.4.

This particular group-velocity matching technique was first demonstrated in an experiment by Mosley *et al.* [43]. The authors employed a frequency-doubled Ti:sapphire laser with 50 fs pulses to pump a pair of 5 mm potassium dihydrogen phosphate (KDP) crystals at 415 nm. For type-II down-conversion in this configuration, the group-velocity of the e-polarized 415 pump field is matched to the o-polarized 830 nm down-conversion photon which theoretically would suffice for the creation of uncorrelated photons. However, the group-velocity matching only holds for a plane wave. In practice, the pump beam has to be focused into the PDC crystal to increase the pair yield and coupling of the down-converted fields into single-mode fibers. This leads to an angular spread of the pump field, which leads to non-ideal group-velocity matching. In [43]

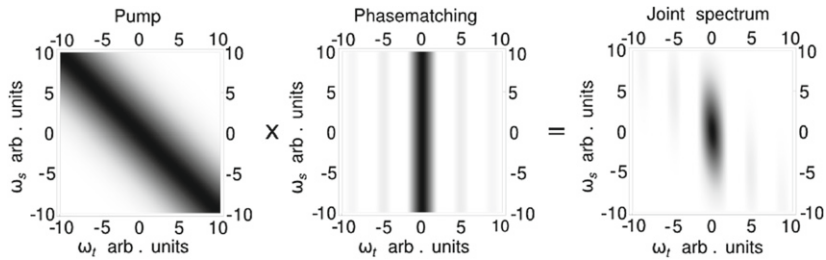

FIGURE 11.10 Group-velocity matching. The condition $v_t' = v_p'$ results in an asymmetric phase-matching function and a vertical, separable joint-spectral amplitude.

this problem was addressed (to some degree) by adjusting the spatial chirp the pump acquired in the frequency-doubling crystal. A detailed analysis of the effects of focusing and spectral pulse shaping can be found in [44].

As a quality benchmark, the authors demonstrated two-photon interference of signal photons created in two independent PDC crystals. This type of experiment was first demonstrated by Hong, Ou, and Mandel [7], and is the basis for many protocols in linear optical quantum information processing. Importantly, the visibility of this two-photon interference is a direct measure of photon-number and spectral purity once the unavoidable spatio-temporal distinguishability in the measurement is accounted for. In [44], the authors achieved an interference visibility of 94.7% for independently heralded photons. The key achievement was that no narrowband spectral filters were used, which usually limit the source brightness in multi-photon schemes.

Symmetric JSA

The second option to attain group-velocity matching is to match the mean group-velocity of the two down-converted fields to the pump group-velocity, $v'_{\mathrm{p}} = (v'_{\mathrm{s}} + v'_{\mathrm{t}})/2$, see Fig. 11.11. This creates a phase-matching function with orthogonal orientation to the pump function. The resulting JSA is thus roughly circular. In order to achieve perfect separability, the widths of the phase-matching and pump functions must be equal, which can be controlled via crystal length or the pump spectrum, respectively [26].

In either case, one can see that the final JSA is still not perfect—the phase-matching function has a distinct sinc shape, which emanates from the integration of the PDC Hamiltonian over a finite crystal length, see Eq. (11.19). The associated side lobes can not be eliminated through group-velocity matching [24]. One way to reduce this residual distinguishability would be to use frequency filtering, but this defies the main purpose of group-velocity matching. Alternatively, one can manipulate the nonlinearity of a PDC crystal to produce a Gaussian-shaped phase-matching function, a technique which has been

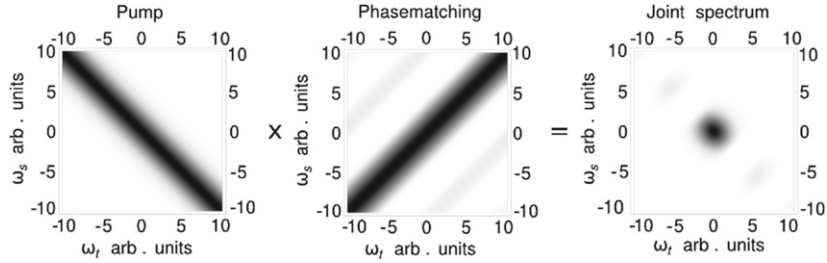

FIGURE 11.11 Group-velocity matching. Setting $v'_{\mathrm{p}} = (v'_{\mathrm{s}} + v_{\mathrm{t}})/2$ creates a symmetric phase-matching function and a circular joint-spectral amplitude.

demonstrated for periodically-poled crystals in [45] and will be outlined in Section 11.4.6.

11.3.2.2 Multiplexed PDC Sources

As shown in Section 11.2.4, the number purity of heralded single photons is strongly dependent on the PDC pump power. The simplest method to reduce multi-photon emission and improve this purity is to operate at lower pump power. This however limits the source brightness, which one cannot always afford. Instead, several sources at lower power can be used in parallel and multiplexed into a single output as discussed above.

In the *spatial* multiplexing scheme suggested in [47], and shown schematically in Fig. 11.12a, several down-converters are run in parallel in a photon switchyard. The efficiency for this scheme was simulated in detail in [46]. It is critically limited by the switchyard architecture and the characteristics of the switches, such as switching time and optical loss.

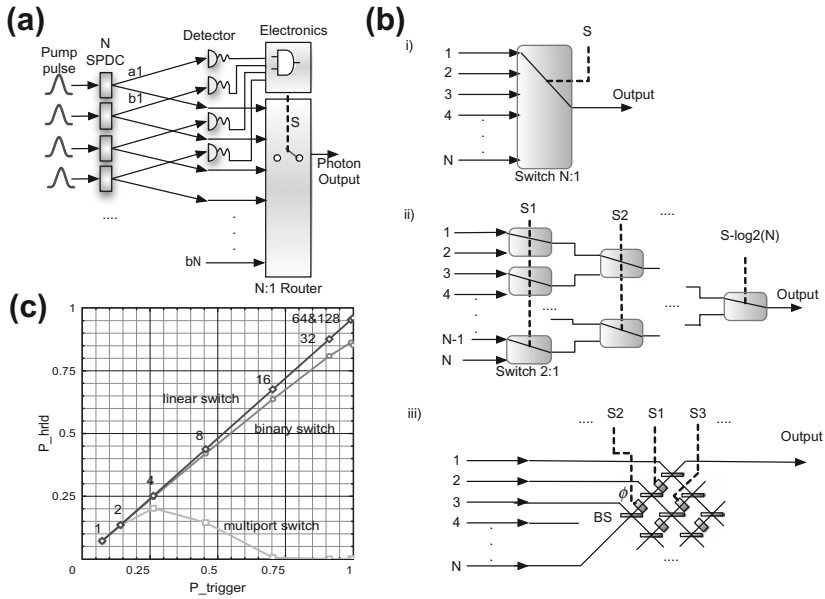

FIGURE 11.12 Heralded photons from spatially multiplexed PDC sources [46]. (a) Tightly synchronized laser pulses pump N PDC sources. One photon from each source is used as a trigger $a_1 \ldots a_N$ while the signal modes $b_1 \ldots b_N$ are routed into the single output mode via an active N:1 switch. (b) Three-photon switchyard configurations are simulated. (i) A single N:1 optical switch; (ii) A succession of 2:1 binary switches; (iii) An all-optical multiport switch. The performance of the multiplexing scheme depends crucially on switching speeds and optical loss in these architectures. (c) Simulation of the three switching schemes, showing the photon heralding efficiency P_{hrld} versus the triggering probability P_{trigger}.

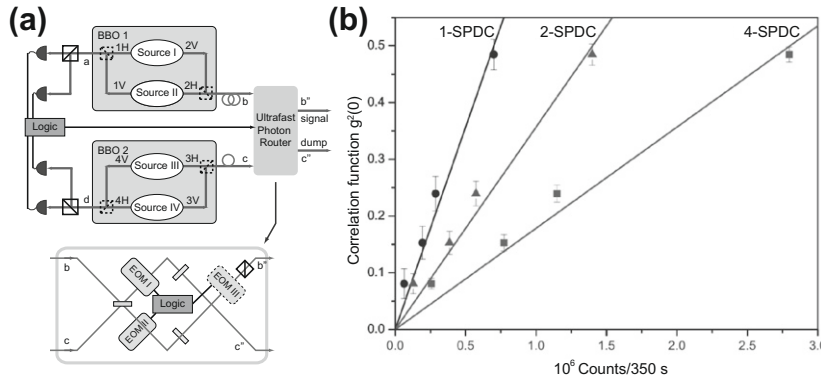

FIGURE 11.13 Demonstration of active PDC multiplexing [34]. (a) Experimental scheme for multiplexing 2 and 4 PDC sources into a common signal mode via fast electro-optical switches (EOM). (b) Correlation function $g^{(2)}(0)$ measured for the multiplexed signal photon. The results show a clear improvement of photon purity for comparable count rates.

Experimentally, this multiplexing scheme has been demonstrated for 2 and 4 PDC sources in [34], see Fig. 11.13. Photon pairs were created in type-II phase-matched BBO crystals. For the 2:1 scheme, one photon of each pair was split off with a polarizing beamsplitter and served as the trigger. The 4:1 scheme was realized with a more sophisticated setup which was based on polarization-entangled photons. The signal photons in both cases were combined with an ultrafast photon router based on electro-optical switches, as shown in Fig. 11.13a. The authors measured the two-photon correlation function $g^{(2)}(0)$ as a benchmark for single-photon purity. The results in Fig. 11.13b show that $g^{(2)}(0)$ for a single PDC source decays quickly toward 1 for high pump powers, where multi-pair emissions dominate. In comparison, the 2:1 and 4:1 multiplexed schemes allow higher pump power and thus higher signal rates for the same $g^{(2)}(0)$, a convincing improvement.

Alternatively, sources can be multiplexed in time. Typically, PDC experiments are pumped with Ti:Sapphire lasers at a fixed pulse repetition rate of 76 MHz, which corresponds to an interval of 13 ns between subsequent pulses. The timing windows for heralded photons can, however, be as small as 1 ns, with the main limitation being the photon detectors and electronics. In this case an experiment could be operated at repetition rates of up to 1 GHz. This would allow operation of a PDC source at lower power, to diminish the number of unwanted higher-order pair emissions, while keeping the signal rate at a reasonable level.

Since the laser repetition rate is usually fixed, it has to be changed externally, as demonstrated in a recent experiment in [48], see Fig. 11.14a. A simple optical delay line, consisting of two beamsplitters and two mirrors, splits off 50% of the frequency-doubled, 76 MHz pump laser and recombines it with the pump mode

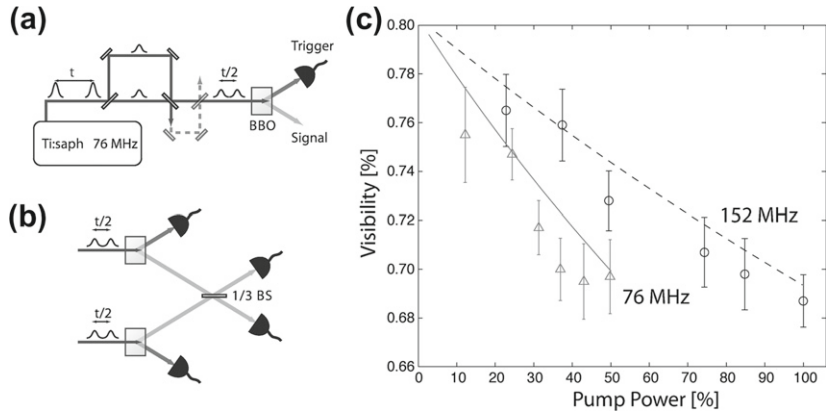

FIGURE 11.14 Temporal multiplexing of PDC sources [48]. (a) The repetition rate of a pump laser can be increased with a simple optical delay line. (b) Two-photon interference on a 1/3 beamsplitter (BS) was used to test the performance of the scheme. (c) The results show that at twice the repetition rate, the interference visibility (which is limited to 80% for this BS) decays by a factor of 2 less with increasing pump power.

after a ≈6.5 ns delay period. The pump repetition rate is doubled to 152 MHz, while the pump power per pulse is reduced to 25%, where 50% of the loss occurs due to the recombination on the second beamsplitter. Usually, this loss can easily be afforded, as state-of-the-art experiments are very efficient and are operated far below the approximately 3–4 W average pump power that can be generated from a frequency-doubled femtosecond Ti:sapph laser. As in [43], this scheme was benchmarked using a two-photon interference experiment between independently generated photons, as shown in Fig. 11.14b. The results in Fig. 11.14c show a clear improvement of the two-photon interference visibility for the doubled repetition rate. The advantage of this temporal multiplexing scheme is that it is simple and can be applied to almost any experiment. The optical delay line can be extended to multiply the repetition rate beyond a factor of 2 without further loss in overall power.

A less complicated alternative for a newly designed experiment would be to employ a pulsed laser with a higher repetition rate. One example would be commercially available picosecond lasers with a repetition rate of 150 MHz. The longer pulse length as compared to femtosecond lasers has some drawbacks, however. Another example are newly available Ti:sapphire femtosecond lasers with up to 1 GHz repetition rate. The overall output power of such a system is considerably lower than for the commonly used 76 MHz Ti:sapphire lasers, but this limitation can be overcome by use of more efficient crystals, as we will see in the next Section 11.4.

Another method to increase the signal to noise ratio of heralded photons, which can be combined with the multiplexing schemes discussed above, is deliberate suppression of unwanted background counts. These background

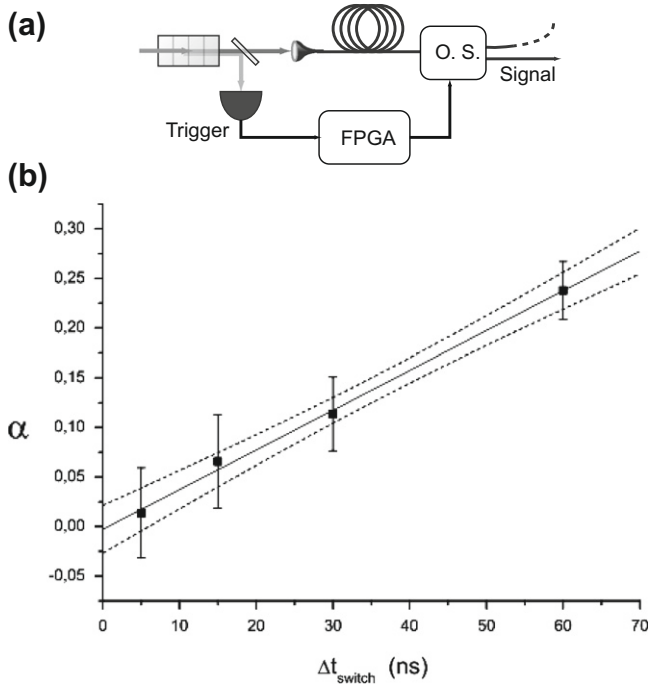

FIGURE 11.15 (a) Scheme for background suppression in heralded PDC [49]. (a) Photon pairs are produced in type-II non-degenerate PDC in a PPLN crystal. The trigger detector synchronizes an optical shutter (O.S.), which blocks the signal line, through a fast field-programmable gate array (FPGA). The 1550 nm signal photon was detected with a InGaAs detector with a timing window of 100 ns. (b) Results. Shorter switching times Δt_{switch} lead to a significant reduction in α, which corresponds to the two-photon correlation function $g^{(2)}(0)$.

counts, either in the heralding or the signal detectors can be intrinsic dark counts caused by the detector, or actual counts induced by background light. The intrinsic dark counts can be minimized by proper choice of detectors (see Chapters 3–7 for an overview).

Extrinsic background counts can be minimized by adding optical shutters to heralded PDC scheme, as demonstrated in [49] and shown in Fig. 11.15. The signal channel in this scheme is blocked until the trigger photon signals the arrival of the signal photon. This technique is especially effective in systems using slow detectors, such as photon-number-resolving transition edge sensors (c.f. Chapter 6). These detectors, due to their high internal jitter, require comparably large coincidence windows ($\approx$100 ns) and operate in a low-count-rate regime. They therefore produce a significant amount of background-induced false-positive coincidence counts, which can be minimized with an optical shutter. The results in Fig. 11.15 show that shutter times below the coincidence timing window increase the single-photon purity.

11.4 PERIODICALLY-POLED CRYSTAL PDC

11.4.1 Quasi-Phase-Matching

Quasi-phase-matching (QPM) was first proposed by Armstrong *et al.* in 1962 [50] to achieve efficient energy transfer between interacting waves in nonlinear media. It is based on a spatial modulation of the nonlinear properties along the propagation direction. The simplest form of QPM is a periodically alternating orientation of the crystal domain, so that the effective nonlinearity flips between $+d_{\text{bulk}}$ and $-d_{\text{bulk}}$ [50]. In contrast to birefringent phase-matching, the interacting fields still propagate with different phase velocities inside the crystal, but when the accumulated phase mismatch reaches π, the sign of the nonlinear susceptibility is reversed. Rather than starting to interfere destructively the fields at this point start at zero phase difference, which then increases again as the fields propagate until it reaches π again, where the nonlinear susceptibility is reversed once more. This creates a step-wise growth in the output power along the crystal length as shown in Fig. 11.16.

We give here a brief introduction of the principles of QPM, a formal derivation of the QPM can be found in [51]. The longitudinally varying nonlinear susceptibility ($d(z)$) can be expressed as a Fourier series

$$d(z) = d_{\text{bulk}} \sum_{\text{m}} G_{\text{m}} \exp(-ik_{\text{m}} z), \tag{11.48}$$

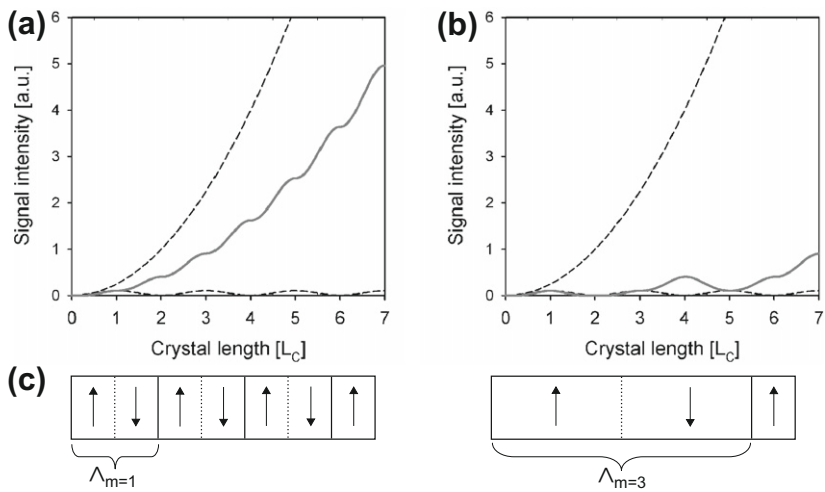

FIGURE 11.16 Solid lines show the effective growth of signal intensity with length in a nonlinear medium (here in units of the coherence length L_{c}) in the case of first-order QPM (a) and third-order QPM (b). The dashed lines show the signal intensity for perfect birefringent phase-matching and the phase-mismatched case. In (c), the poling structure and periodicity Λ are schematically drawn for the first- and third-order cases.

where d_{bulk} is the nonlinear coefficient of the bulk material, G_{m} are the Fourier coefficients, $k_{\text{m}} = 2\pi m/\Lambda$ is the grating vector of the m-th Fourier component, and Λ is the spatial period of the modulated structure.

Assuming that only one Fourier component is phase matched and contributes significantly to the PDC process, the integration of the signal amplitude from Eq. (11.9) yields

$$E_{\text{s}} \propto L\, d_{\text{Q}}\, \text{sinc}\left(\Delta k_{\text{Q}}\, \frac{L}{2}\right), \tag{11.49}$$

where d_{Q} is the effective nonlinear coefficient in QPM. For a square-wave modulation of the nonlinearity from $+d_{\text{bulk}}$ to $-d_{\text{bulk}}$ the effective nonlinear coefficient becomes:

$$d_{\text{Q}} = 2\, d_{\text{bulk}}\, \sin(\pi\ D)/m\ \pi, \tag{11.50}$$

where the duty factor $D = l/\Lambda$ is given by the length l of a single reversed domain divided by the period Λ. The value of m determines the order of the QPM. As the efficiency of the nonlinear process is proportional to $1/m^2$, a low-order QPM is desired. However this comes with the price of small periodic structures (Λ). For example, in a first-order QPM (Fig. 11.16) the period Λ has to be twice the coherence length l_{c} as defined in the bulk medium, see Eq. (11.10). The largest nonlinear coefficient for QPM is obtained for a first-order process with duty cycle of 50%. In this case

$$d_{\text{Q}} = \frac{2}{\pi} d_{\text{bulk}}. \tag{11.51}$$

The effective nonlinearity in QPM is therefore reduced by at least a factor of $\frac{2}{\pi}$ compared to the value for birefringent phase-matching in the bulk medium.

The Hamiltonian in Eq. (11.21) has the following form for QPM:

$$\int_{t_0}^{t} \text{d}t\ \hat{H}_{\text{PDC}}(t') = 2\pi\ B\, d_{\text{Q}} \iint \text{d}\omega_{\text{s}}\, \text{d}\omega_{\text{t}}\, \alpha(\omega_{\text{s}} + \omega_{\text{t}}) \times L\ \text{sinc}\left[\Delta k_{\text{Q}} \frac{L}{2}\right] \hat{a}_{\text{s}}^{\dagger}(\omega_{\text{s}}) \hat{a}_{\text{t}}^{\dagger}(\omega_{\text{t}}) + h.c.. \tag{11.52}$$

The effective wave-vector mismatch due to the quasi-phase-matching is

$$\Delta k_{\text{Q}} = k_{\text{p}} - k_{\text{s}} - k_{\text{t}} - k_{\text{m}} = \Delta k_{\text{bulk}} - k_{\text{m}}, \tag{11.53}$$

assuming that all wave vectors are collinear with the grating vector. The grating vector is a powerful parameter as it is independent of material properties and can be easily adjusted during crystal fabrication, as shown in the periodic-poling section below. Even if the wave-vector mismatch is non-zero for the bulk material, using quasi-phase-matching a fully phase-matched interaction

($\Delta k_Q = 0$) can be achieved for maximum conversion efficiency. In addition, the phase-matching can be tuned (somewhat) using the temperature dependence of the refractive index, with the wave vector k given by

$$k(\lambda, T) = \frac{n(\lambda, T)\omega}{c}. \tag{11.54}$$

The grating vector k_m is also affected by temperature changes, since the poling period $\Lambda(T)$ depends on the thermal expansion of the medium. The temperature and wavelength dependence of the refractive index can be easily derived using the empirical Sellmeier equations of the medium, e.g., for potassium titanyl phosphate (KTP), the Sellmeier coefficients can be found in Refs. [52,53].

The QPM approach has several advantages over the birefringent phase-matching discussed in the previous chapter:

- Free choice of the trigger and signal wavelengths by appropriate choice of the modulation period Λ.
- For fixed choice of trigger and signal wavelength, the propagation direction of trigger and signal photons can be made collinear with the pump photons, eliminating spatial walk-off effects in the transverse direction.
- With no walk-off, the interaction length inside the nonlinear medium can be very long, increasing the conversion efficiency.
- Free choice of polarization of the pump, trigger, and signal fields. This allows to make use of the largest component of the nonlinear susceptibility tensor to maximize conversion efficiency in a given nonlinear medium.
- Easy tunability of the trigger and signal wavelengths of several nm by controlling the temperature of the nonlinear medium.
- Complex phase-matching conditions can be achieved by using non-periodic modulation of the nonlinear coefficient.

The advantage of QPM is illustrated in Fig. 11.17 where different phase-matching scenarios are realized in the same nonlinear medium, a periodically-poled KTP (ppKTP) crystal. The top row shows data from a simulated type-II phase-matched ppKTP, with signal and trigger wavelengths around 810 nm. The trigger and signal wavelengths for collinear emission are plotted against the poling period, temperature, and pump wavelength. By simply varying the period of the poling, the difference in wavelength can be altered at will around the degeneracy wavelength of 810 nm (set by the pump wavelength) which occurs at $\Lambda = 10.7$ μm. Although not as strong, the additional dependence of the phase-matching on temperature is very helpful in experiments since it allows fine tuning of the trigger and signal wavelengths to match existing filters or atomic absorption lines without interfering with the optical setup. If a tunable pump is available, fine tuning can also be achieved using different pump

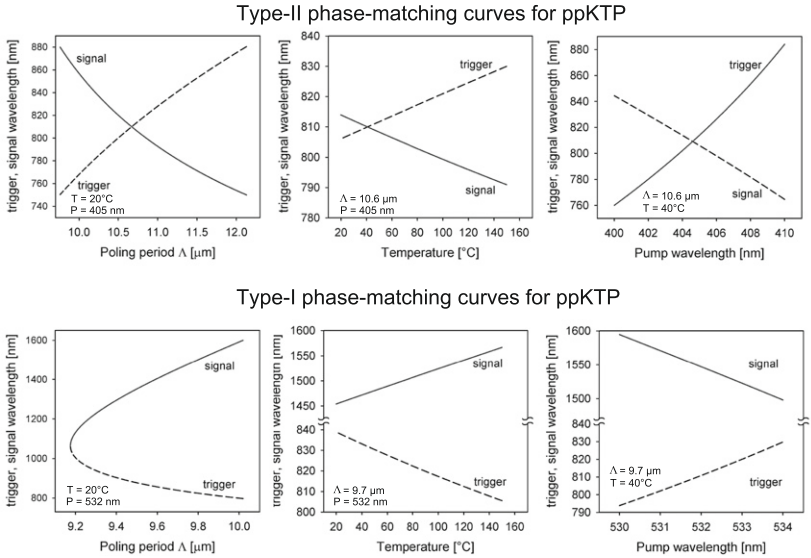

FIGURE 11.17 Simulated phase-matching curves of ppKTP using SLNO (Select Nonlinear Optics (software), by Dr. Arlee Smith, download: http://www.as-photonics.com). The first row shows the phase-matching conditions for a degenerate type-II interaction as functions of three parameters: poling period Λ, temperature, and pump wavelength. The second row shows a non-degenerate type-I interaction.

wavelengths, as shown on the right-most plot. The bottom row of Fig. 11.17 shows a simulation for the same ppKTP crystal but this time phase-matched for type-I with non-degenerate signal and trigger wavelengths. By slightly changing the poling period to $\Lambda = 9.9\ \mu\text{m}$, the crystal (at 20°C) produces trigger and signal photons at highly non-degenerate wavelengths. The trigger is found at 810 nm and the signal lies at 1550 nm, a wavelength combination that profits from the high available detection efficiency at 810 nm and low transmission losses at 1550 nm in optical fibers. The same wavelength pair can be obtained from a crystal with period $\Lambda = 9.7\ \mu\text{m}$ when heated to about 130°C, as shown on the bottom center of Fig. 11.17.

Note that there is no crossing of the trigger and signal wavelengths at the degeneracy point, as in the type-II case. Since in type-I both photons have the same polarization they become indistinguishable and interchangeable at degeneracy. As a result the natural bandwidth of trigger and signal at degeneracy is larger for type-I phase-matching.

Even if the period Λ is fixed after production of the crystal, the exact wavelengths for collinear emission can still be tuned using either the crystal temperature or pump wavelength. It is clear that this technique provides the experimenter with very valuable additional controls when operating or designing an experimental setup.

11.4.2 Periodic Poling

The spatial modulation of the nonlinearity can be realized in ferroelectric crystals by periodically altering the crystal orientation so that the effective nonlinearity alternates between $+d_{\text{bulk}}$ and $-d_{\text{bulk}}$ in each domain. An early method for generating domain reversal was periodic modulation during crystal growth, but this approach lacked precise control of the domain size over long distances. Later use of lithographic methods improved the control of the domain structure. In this technique, a lithographic mask is used to define the periodic-poling regions after crystal growth. Initially the first periodic poling under lithography was based on in-diffusion of dopants [54] or through ion exchange [55]. However these methods could only produce periodically-poled waveguides because the domains only penetrated a few μm into the substrate. Finally, electric-field poling methods, developed in the early 1990s, enabled the production of bulk periodically-poled structures for high-power applications [56–58].

In electric-field poling the nonlinear medium is lithographically patterned with electrodes. A pulsed electric field is then applied to the electrodes, and if the field is strong enough, spontaneous reversal of the crystal structure occurs. The critical field strength at which poling occurs is called the coercive field. The actual value for the critical field depends on the crystal properties and is on the order of several kV/mm. By reversing the domains only under the electrodes, see Fig. 11.18, a periodic structure with alternating nonlinearity is achieved.

One of the first demonstrations of PDC in a periodically-poled bulk crystal was performed by Mason *et al.* in 2002 [59], where a periodically-poled lithium niobate (ppLN) crystal was used to generate photon pairs at 800–1600 nm. Although waveguide experiments preceded bulk operation in this instance, due to the easier fabrication of periodically-poled structures in small surface layers, the number of PDC experiments based on periodically-poled bulk-crystals grew rapidly thereafter [60–62]. The early experiments were not entirely directed toward the creation of heralded single photons, but many of them already revealed the need for efficient coupling and photon-number purity.

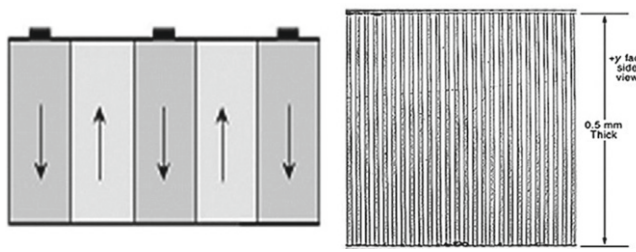

FIGURE 11.18 Left: Domain reversal underneath the electrode region. Right: Uniform 15 μm wide domain structure through a 0.5 mm thick crystal. *Reprinted figure with permission from D.S. Hum and M.M. Fejer, Comptes Rendus Physique 8, 180–198 (2007). Copyright © 2007 Acadmie des sciences. Published by Elsevier Masson SAS. All rights reserved.*

The following sections of this chapter discuss strategies for efficient coupling of the output fields to optical fibers and detail the experimental effort to achieve high photon-number purity and spectral purity with periodically-poled PDC sources.

11.4.3 Optimal Focus Parameters for Heralding Efficiency

In most instances, trigger and signal photons produced inside the nonlinear medium will be coupled to single-mode fibers (SMF), in order to guide them to the analysis and detection stations. In particular, the ability to tune the PDC to collinear emission makes the use of single-mode fibers very attractive since the trigger and signal photons can be coupled very efficiently. The key parameters for a single-photon source are heralding efficiency and the overall rate of heralded photons. The heralding efficiency ($\eta_{s|t}$) is defined as the probability of a signal photon being in the single-mode fiber given the detection of a trigger photon. Since single-photon detectors can have efficiencies ranging from $< 1\%$ to above 90%, it is difficult to compare the heralding efficiency when different types of detectors are used. Therefore the detection efficiency has been excluded from the values of the heralding efficiencies stated below for easier comparison.

Several theoretical and experimental investigations have been conducted to find the optimal fiber-coupling configurations [63–67]. In Fig. 11.19, taken from [64], a non-degenerate PDC source for heralded photons is depicted that produces trigger photons at 810 nm and signal photons at 1550 nm. A laser is focused at the center of the ppLN crystal with a focal spot waist size of W_p.

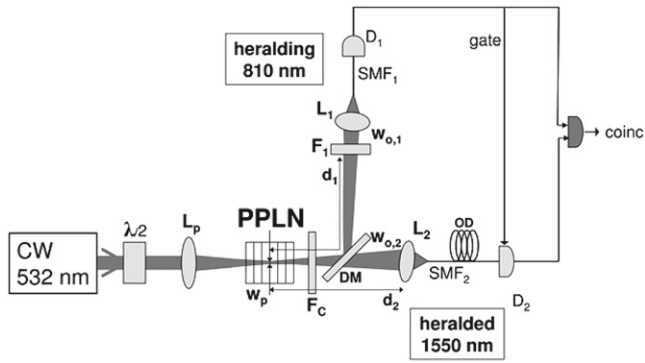

FIGURE 11.19 Setup for production of heralded single photons at 1550 nm. The pump beam is focused to a waist size of W_p inside a 5 mm long ppLN crystal. The fiber cores have waist sizes of $W_{o,1}$ and $W_{o,2}$ for trigger (810 nm) and signal (1550 nm) photons, respectively. In the main text these waists are refereed to as W_t and W_s. *Reprinted figure with permission from S. Castelletto, I.P. Degiovanni, V. Schettini, and A. Migdall, Metrologia, 43, S56-S60, 2006. © Bureau International des Poids et Mesures. Reproduced by permission of IOP Publishing. All rights reserved.*

Likewise the mode accepted by the optical fibers is also imaged at the same location as the pump beam, generating two waists W_t and W_s, for the trigger and signal fiber, respectively. Note that the size of the mode field in the fibers is dependent on the wavelength and therefore W_t and W_s are not necessarily the same.

Measurements of $\eta_{s|t}$ were performed at a fixed $W_p = 144$ μm and a fixed $W_t = 82$ μm for two different signal waists (W_s). Spectral filtering was achieved solely by the geometrical acceptance of the single-mode fibers and a FWHM of ≈2 nm was measured for the trigger photon. For W_s of 158 μm and 197 μm the measured heralding efficiencies were 16% and 21%, respectively. Much higher heralding efficiencies were obtained by using a narrow band filter ($\Delta\lambda = 0.1$ nm) in the trigger path. In this case the efficiency increased nearly to unity when optical losses were removed.

A thorough theoretical model for the case of non-degenerate PDC at 810–1550 nm devised by Ljunggren *et al.* [63] came to a similar conclusion: when a narrow filter is applied to the trigger field the heralding efficiency can reach up to 100% over a large range of focusing conditions, as shown in Fig. 11.20. Narrow filtering in this context means a reduction of the bandwidth of the photons below the bandwidth limit set by the crystal properties and collection angle of the SMF. The focusing parameters in Fig. 11.20 are not directly given in waist sizes but are defined as $\xi = L/z_R$, the ratio between crystal length L and the Rayleigh-range z_R of a standard Gaussian beam. This representation is helpful as it turns

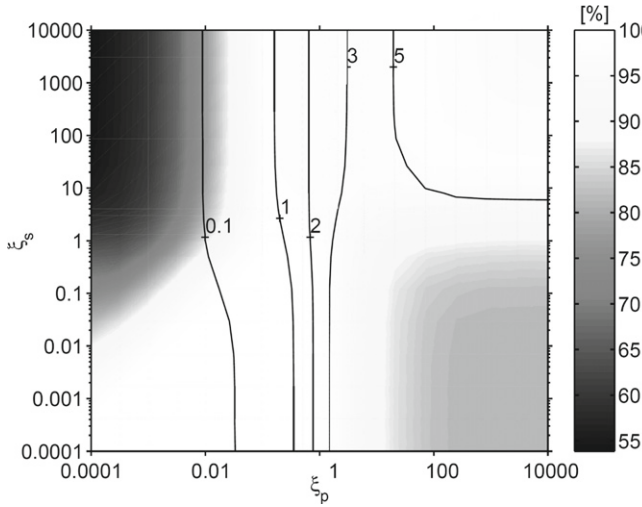

FIGURE 11.20 Plot of maximally achievable heralding efficiencies ($\eta_{s|t}$) as function of focusing parameters for pump and trigger modes (ξ_p,ξ_t). Black lines indicate the optimal signal focusing conditions (ξ_s) in order to maximize $\eta_{s|t}$. *Reprinted figure with permission from D. Ljunggren and M. Tengner, Phys. Rev. A, 72, 062301, 2005. Copyright (2005) by the American Physical Society.*

out that the optimal focusing parameter ξ^{opt} is independent of the crystal length. It is also interesting to see that the exact values of the individual modes is not very important because the maximum for the heralding efficiency is very broad, (note the logarithmic scale for ξ_p and ξ_t). As a rule of thumb, a large heralding efficiency is expected when the ξ's of all three fields are on the order of one, i.e., when the crystal length is about twice the Rayleigh range. Experimental data was also obtained using a 4.5 mm ppKTP crystal phase-matched to 810–1550 nm. A heralding efficiency, excluding all optical losses, of 34% was reported with focusing parameters of $\xi_p = 2.1$, $\xi_t = 3.2$ and $\xi_s = 2.5$.

Another interesting finding of [63] is the dependence of the fiber-coupled photon rate, and hence the heralding rate, on the crystal length, when operating at optimal focusing. With no additional spectral filtering, only the fiber acts as a frequency filter and the coupled photon rate R scales as

$$R(\Delta\lambda_{\text{wide}}) \propto \sqrt{L}, \tag{11.55}$$

whereas in the case of narrow filtering the dependence goes as

$$R(\Delta\lambda_{\text{narrow}}) \propto L\sqrt{L}. \tag{11.56}$$

The reason for the smaller growth of the rate with crystal length, as compared to Eq. (11.49), is the focusing of the pump beam. The angular spread in pump k-vectors generates additional sinc functions that are slightly offset, causing the spectral width to decrease as $1/\sqrt{L}$ with the crystal length.

Another experimental study investigated optimal focusing parameters for the case of degenerate PDC around 810 nm [65]. Absolute coincidence rates and heralding efficiencies were measured for varying pump and signal/trigger waist sizes. The main findings are shown in Fig. 11.21 for a 15 mm long ppKTP crystal. For this crystal the maximum heralding efficiency was measured to be

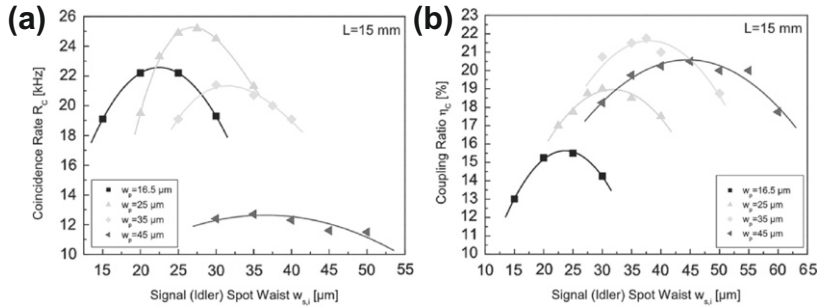

FIGURE 11.21 Coincidence count rates (a) and heralding efficiencies ($\eta_{s|t}$) (b) for a 15 mm long ppKTP for a series of focusing conditions. *Reprinted figure with permission from A. Fedrizzi, T. Herbst, A. Poppe, T. Jennewein, and A. Zeilinger, Opt. Express, 15, 15377-15386, 2007. Copyright (2007) by OSA.*

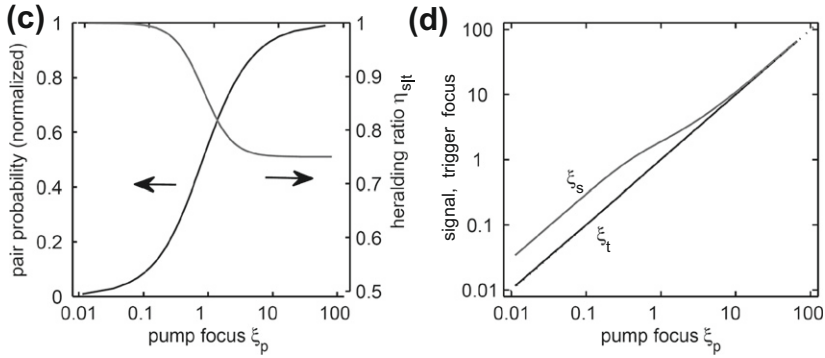

FIGURE 11.22 Simultaneous optimization of the total collection probability and heralding efficiency $\eta_{s|t}$. Panel on the right shows the focusing parameters which result in the best trade-off between collection probability and heralding efficiency. *Reprinted figure with permission from R.S. Bennink, Phys. Rev. A, 81, 053805, 2010. Copyright (2010) by the American Physical Society.*

around 22% for single-mode coupling without any additional filtering of the signal/trigger fields.

The reader should note that the optimal focusing conditions are different for maximal rate and maximal heralding efficiency. The optimum heralding efficiency is achieved with a looser focusing, enabling a higher mode overlap of the signal and trigger modes at the optical fiber. Other crystal lengths, ranging between 10 and 25 mm, were also investigated showing the independence of the focusing parameter ξ^{opt} with crystal length for the signal and trigger fields. The square-root dependence of the fiber-coupled photon rate given in Eq. (11.55) was also verified experimentally in this investigation.

In a recent theoretical work by Bennink [66], the trade-off between maximal pair rate and heralding efficiency was also found. Contrary to [63], Bennink assumed collinear Gaussian spatial modes. The calculation proceeds to find the various probabilities that the trigger and signal fields are emitted into collinear Gaussian modes. Such Gaussian modes can be coupled very efficiently to single-mode optical fibers and therefore the analysis can be regarded as if the trigger and signal fields are fiber coupled. The theoretical results for the heralding efficiency are summarized in Fig. 11.22.

It is evident from the figure that with a strong pump focus ($\xi_p \gg 1$) there will be a high overall pair-coincidence rate. However the trigger and signal might not be emitted into the same modes, and therefore the heralding efficiency will be decreased. In the limit of a weak pump focus ($\xi_p \ll 1$) the trigger and signal fields are in the same mode and have a higher heralding efficiency. No closed forms for ξ_t and ξ_s are given for the maximum values of $\eta_{s|t}$, but the right plot in Fig. 11.22 displays the values of ξ_t and ξ_s, which results in the best trade-off between collection probability and heralding efficiency. Nevertheless the study shows that near unity heralding efficiencies are possible

when the pump beam is weakly focused. A recent experimental investigation corroborated these findings by reporting a heralding efficiency of 84% in a 25 mm long ppKTP crystal [68]. This result was achieved with a weakly focused pump ($\omega_p = 200\ \mu m$) and more strongly focused trigger and signal modes ($\omega_{t,s} = 175\ \mu m$). When comparing results, one should note that in [66] the focus parameter is defined as $\xi = \frac{L}{2z_R}$, which is half the size of the definition in [63] for the same focusing condition.

Similar heralding efficiencies were reported in [69,70]. Both these setups are based on a ppKTP crystal phase-matched for creation of photon pairs at 810 nm from a 405 nm pump laser, and both used the results from [65,66] for optimal focusing. A heralding efficiency of 80% was observed in [69]. In [70] a standard telecom fiber (SMF-28), guiding two spatial modes at 810 nm, was used to increase the coupling efficiency of the signal photon. The larger mode field diameter of the SMF-28 fiber increased the heralding efficiency to 87%. Both experiments also employed transition-edge sensors (TES) with $\eta_{DE} > 95\%$ to achieve high heralding efficiencies, including detection.

11.4.4 Number Purity

As outlined in Section 11.2.4, the photon state produced by PDC contains terms with more than one trigger/signal pair. These higher-order pairs lead to a degradation of the purity of the single-photon signal, especially when a non-number resolving detector is used to herald the presence of the signal. Without using the elaborate schemes of switched PDC sources presented at the end of Section 11.2.4 it is possible to approximate a single-photon state using a weakly pumped heralded PDC source. The photon-number purity can be measured using a Hanbury Brown-Twiss setup in the signal arm. Without heralding, the signal photons of a single-mode PDC beam have thermal statistics [71], i.e., it shows bunching of photons with an increased probability that two or more signal photons are detected at the same time. In the heralding case, these measurements are conditioned on the detection of a trigger photon so that the second-order correlation function ($g_c^{(2)}$) of the signal arms becomes [72]

$$g_c^{(2)}(t_1,t_2|t_t) = \frac{\langle \hat{E}_s(t_1)\,\hat{E}_s(t_2)\,\hat{E}_s^\dagger(t_2)\,\hat{E}_s^\dagger(t_1)\rangle_c}{\langle \hat{E}_s(t_1)\,\hat{E}_s^\dagger(t_1)\rangle_c\,\langle \hat{E}_s(t_2)\,\hat{E}_s^\dagger(t_2)\rangle_c}, \tag{11.57}$$

where $\hat{E}_s(t), \hat{E}_s^\dagger(t)$ are the field operators for the signal arm at times t_1 and t_2. The average $\langle \ldots \rangle_c$ is conditioned on the detection of a trigger photon at time t_t. If a PDC source is used for the production of single photons, we are especially interested in the probability of a second signal photon at time $t_2 = \tau$, given that a signal photon at $t_1 = 0$ was heralded by the detection of a trigger photon at $t_t = 0$. In this case the second-order correlation function reduces to: $g_c^{(2)}(0,\tau|0)$.

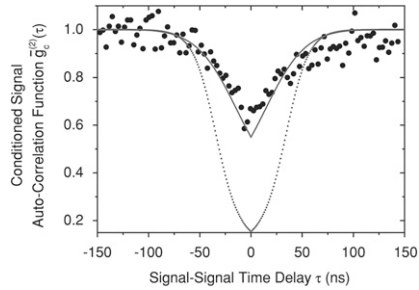

FIGURE 11.23 Measured (dots) and simulated (solid line) second-order coherence function of signal photons conditioned on the detection of a trigger photon. The dotted line represents a simulation without background noise. (For interpretation of the references to color in this figure legend, the reader is referred to the web version of this book.) *Reprinted figure with permission from D. Höckel, L. Koch, and O. Benson, Phys. Rev. A, 83, 013802, 2011. Copyright (2011) by the American Physical Society.*

In Fig. 11.23, this correlation is plotted and clearly shows a dip below unity around $\tau = 0$.

It is thus possible to obtain anti-bunched light from a PDC source, and therefore a suppression of higher photon-numbers, even though the individual signal and trigger fields show thermal (bunching) statistics. This is possible since the heralding uses the very strong non-classical correlations between the two fields (pair generation), which is independent of pump power. On the other hand, the probability to detect two signal photons, which scales quadratically with the pump power (see Eq. (11.40)), can be made arbitrarily small by reducing the pump intensity. It should be noted that the simple heralding presented here approximates a single-photon state with $g_c^{(2)}(0) = 0$ only in the limit of negligible pump power and heralding rate. To obtain single-photon statistics at high rates, one has to revert to the switched PDC scheme as outlined in Section 11.2.4, or some other technique.

Several experimental investigations have observed the antibunching feature of the signal photons when conditioned on the trigger [72–77]. In [72] a cw pumped 10 mm long ppKTP crystal was used to produce trigger and signal photons around 800 nm. A conditioned measurement of the signal second-order correlation function yielded $g_c^{(2)}(0) = 0.7$ at a heralding rate of $\approx$240,000 s^{-1}. A suppression of higher photon-numbers by 2 orders of magnitude compared with a Poissonian light source ($g_c^{(2)}(0) = 0.01$) was reported by [75], although in this instance the heralding rate was reduced to $\approx$5000 s^{-1}. This experiment is also interesting because it used cavities around the ppKTP crystal to enhance the coherence time of the photons to beyond 140 ns. In this regime the detector jitter is negligible and the shape of the coherence function is given by the temporal extent of the wavepacket alone. The lowest $g_c^{(2)}(0)$ for single-photon sources based on PDC was reported in [77] with a value of 0.005.

11.4.5 Spectral Purity

To have spectrally independent trigger and signal photons, Eq. (11.38) has to be fulfilled, which states that the group-velocity of the pump in the nonlinear medium must lie between the group-velocities of the trigger and signal fields. In the visible wavelength range this requirement is difficult to satisfy since the normal material dispersion at lower (pump) wavelengths results in lower group-velocities for the pump. However, by moving to longer wavelengths the differences in dispersion between pump, trigger, and signal fields become small. It is then possible, by including the dependence of the group-velocity with polarization, to find a solution in which the orthogonally polarized trigger and signal fields have group-velocities above and below the pump [78]. For example, in type-II PDC using KTP, it is possible to match the group-velocities in a pump wavelength range of 650–900 nm, corresponding to degenerate wavelengths of 1300–1800 nm for the trigger and signal fields. In an experiment by Evans *et al.* [79] a pump wavelength of 776 nm was used to produce trigger and signal pairs at 1552 nm in a 20 mm long type-II ppKTP. In addition, the crystal was periodically-poled to yield zero phase mismatch at those wavelengths. To obtain the minimal spectral entanglement a specific width of the pump spectrum had to be chosen, corresponding to a pulse duration of 1.3 ps. Joint-spectral intensities were measured and can be seen in Fig. 11.24a. Analysis of the spectrum yields a spectral Schmidt number of 1.07, indicating a very high spectral purity of the trigger and signal photons.

Spectral purity of trigger and signal photons has also been shown in an experiment using a periodically-poled KDP crystal, quasi-phase-matched for

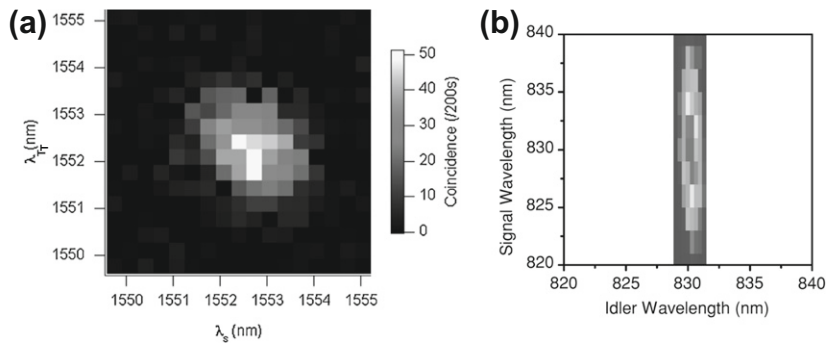

FIGURE 11.24 Joint-spectral intensity of the trigger and signal modes in (a) type-II ppKTP crystal pumped at 776 nm. *Reprinted figure with permission from P.G. Evans, R.S. Bennink, W.P. Grice, T.S. Humble, and J. Schaake, Phys. Rev. Lett., 105, 253601, 2010. Copyright (2010) by the American Physical Society.* and (b) type-II ppKDP crystal pumped at 415 nm. *Reprinted figure with permission from R.-B. Jin, J. Zhang, R. Shimizu, N. Matsuda, Y. Mitsumori, H. Kosaka, and K. Edamatsu., Phys. Rev. A, 83, 031805, 2011. Copyright (2011) by the American Physical Society.*

type-II PDC [80]. The trigger and signal fields were degenerate at 830 nm and their joint-spectral intensity can be seen in Fig. 11.24b. The Schmidt value obtained from the experimental data was 1.03, demonstrating again the high spectral purity.

11.4.6 Non-Uniform Periodic Poling

The versatility of poled structures is further increased through transversal or longitudinal patterning of the quasi-phase-matched poling structure. Transversal patterning can be used to control the spatial component of the PDC biphoton wave function, see e.g., [81,82]. Longitudinal patterning enables the manipulation of the spectral PDC wavefunction, which is arguably more important for the purpose of creating pure heralded single photons. A linearly-chirped poling period $\Lambda(z)$, for example, allows the creation of ultra-broadband single photons for optical coherence tomography [83]. A longitudinal, interleaved superposition of multiple poling periods may lead to quasi-phase-matching solutions for multiple sets of wavelengths [84], or for concurrent type-0, type-I and type-II PDC [85].

Longitudinal domain engineering can be used to address one of the remaining problems not addressed by group-velocity matching. In a standard PDC experiment, wavepackets have a sinc frequency spectrum. As can be seen from Eq. (11.19), this is due to the fact that a crystal has finite length and a rectangular shape—the nonlinear interaction between the pump beam and the crystal is thus turned on abruptly to its full strength when the pump enters the crystal, and remains constant until it is turned off when the pump exits the crystal. In the frequency domain, this temporal step-function transforms into a sinc shape, see Eq. (11.20). This spectral shape causes residual frequency distinguishability even in the presence of group-velocity matching—see the sidelobes in Figs. 11.10 and 11.11—which has a detrimental effect on the purity of heralded PDC photons [24].

To fully reduce these side lobes, the constant nonlinearity of the crystal must be turned into an effective Gaussian function. In [45], a 10 mm ppKTP was longitudinally patterned with discrete sections of increasingly higher-order polings, see Fig. 11.25. The pump beam entering the crystal first encountered a section with poling order $m = 32$, experiencing, according to Eq. (11.50), a very weak effective nonlinearity. The nonlinearity was then increased step by step, peaking at $m = 1$ in the crystal center and then dropping off symmetrically. The theoretic biphoton spectrum obtained with this spectral engineering method, shown in Fig. 11.25b, was confirmed by measuring two-photon interference patterns, which showed a distinctly Gaussian pattern instead of the characteristic triangular pattern of sinc^2-shaped bi-photons.

Combining these engineered nonlinearities with group-velocity matching leads to a significant improvement in photon purity without the need for spectral filtering, as shown numerically in [45].

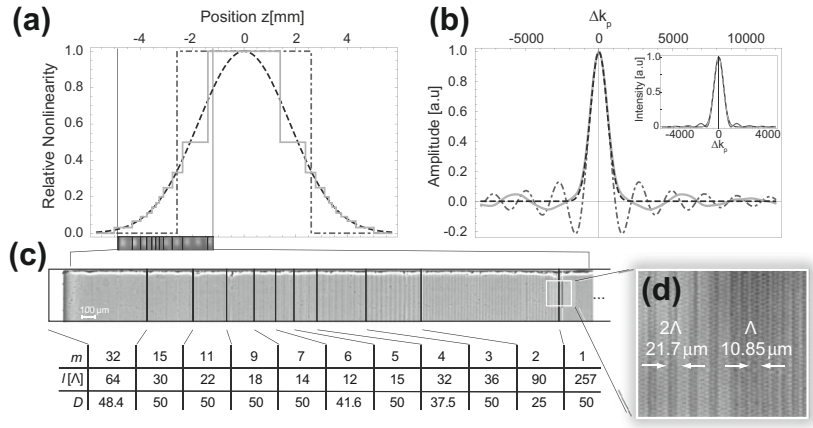

FIGURE 11.25 Spectral biphoton shaping via engineered crystal nonlinearities *(Reprinted figure with permission from A.M. Brańczyk, A. Fedrizzi, T.M. Stace, T.C. Ralph, and A.G. White, Opt. Express, 19, 55–65, 2011. Copyright (2011) by OSA.)*. (a) A Gaussian nonlinearity profile (black dashed line) was approximated with discrete crystal sections (gray solid line) of order m. (b) Phase-matching function amplitudes and intensities (inset) for the aperiodically poled crystal (solid line) compared to a ppKTP of the same effective length (dot-dashed line) and target Gaussian profile (dashed line). (c) Magnified image of part of the custom crystal. Vertical lines separate sections with constant nonlinearity, with their poling order, length L and poling duty cycle D. (d) Zoom into the transition from poling order $m = 1$ to $m = 2$.

11.5 WAVEGUIDE-CRYSTAL PDC

After the success of PDC in bulk crystals as a source of heralded single photons (see Section 11.3) and the incorporation of periodic poling for quasi-phase-matching enabling easy tunability of the signal and trigger wavelengths (see Section 11.4) another major development was the inclusion of waveguide technology, as depicted in Fig. 11.26.

The confinement of the electric fields inside a waveguide leads to extremely high field amplitudes in the nonlinear material, increasing the down-conversion rate by several orders of magnitude in comparison to bulk-crystal sources.

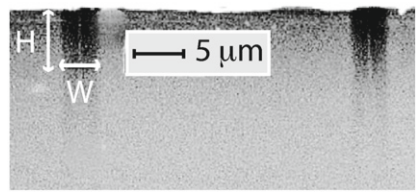

FIGURE 11.26 Microscopy of the waveguide used in [86] (color adjusted). The depicted cross-section gives an impression of the tooth-like waveguide structure and enables a rough estimate of its dimensions.

Furthermore the confinement of the signal and trigger fields in the waveguide modes enables efficient coupling to optical fibers. Finally, waveguided PDC allows for the integration into small-scale devices that may include sources, optical circuits, and detectors.

11.5.1 History and Experimental Implementations

The main challenge for the generation of heralded single photons in nonlinear waveguides is the production of high-quality waveguides with low losses and minimal variation over the length of the structure. There are several materials available that are well suited for nonlinear optical waveguides, including dielectric materials such as lithium niobate ($LiNbO_3$ or LN), lithium tantalate ($LiTaO_3$), potassium titanyl phosphate ($KTiOPO_4$ or KTP) [87,88], and potassium niobate ($KNbO_3$) [14]. Nonlinear semiconductor materials include AlGaAs, GaAs, ZnSe, ZnTe, and InP [89–92]. In comparison to dielectric materials, semiconductors feature higher nonlinearities, but also higher loss rates.

The methods to create waveguiding structures inside the nonlinear materials are as varied as the materials, ranging from proton exchange, anneal/proton exchange over ion exchange, to metal-diffused waveguides (Ti-, Rb-, Zn-indiffusion), ion-implantation waveguides, and epitaxial-growth methods. Each method has its inherent advantages and disadvantages. For example ion-exchange waveguides in LN guide only one polarization, but allow burying the waveguide in the material via reverse-proton-exchange processes. To perform type-II PDC in LN one has to resort to metal-diffused LN waveguides, which guide both polarizations but are always located at the surface. There exists an extensive literature on the waveguide production process, with an overview given in [14].

The most commonly used waveguide materials for PDC are LN and KTP, which gained popularity due to their low losses, special dispersion properties, and ease of fabrication. The first photon-pair PDC source using waveguides was presented in 2001 by Tanzilli *et al.* [93] in LN, and already featured down-conversion rates four orders of magnitudes higher than bulk-PDC sources at that time. Soon afterwards the spatial properties of PDC in waveguides were investigated [94]. Since then a lot of improvements were made to this process [95–97]. The generation of type-II PDC in a waveguide yielded signal and trigger states in orthogonal polarizations, such that they could be separated by a polarizing beam splitter and efficient state generation could be accomplished [26,98,99]. Nonetheless, all these sources created frequency-correlated photon pairs, resulting in the heralding of mixed single-photon states. Frequency filtering of photon-pair states for producing pure single-photon Fock states was experimentally investigated in [25].

The first direct production of uncorrelated photon pairs in waveguides based on group-velocity matching [100] was demonstrated in 2011, two years after

the initial breakthrough by Mosley *et al.* relying on bulk PDC [43], and ten years after the first demonstration of waveguided PDC [93]. Since then the available generation rates and heralding efficiencies have continuously improved [101]. Modern sources exhibit heralding rates up to 80% and feature high conversion efficiencies [102].

One advantage of PDC in waveguides for heralded Fock-state generation is the fact that it opens up new possibilities to achieve uncorrelated photon-pair generation. For example, Bragg structures placed at the boundaries of the waveguide can be used to modify the dispersion properties inside the waveguides, enabling group-velocity matching in various materials and at wavelengths previously not available due to their unfavorable material parameters [103]. Waveguides also enable the creation of counterpropagating photon pairs, in which one photon travels backward toward the pump [104, 105,27]. This setup, while technologically challenging, leads to uncorrelated photon-pair emission that is (almost) independent of the dispersion properties of the crystal material.

11.5.2 Theory of PDC in Waveguides

To mathematically describe the PDC process in waveguides we expand the theory presented in Section 11.2 to include the transverse degrees of freedom, as in Section 11.3, while also including the effects of an optical guide.

To calculate the two-photon state emitted by the process of waveguided parametric down-conversion (see Fig. 11.27) we extend the PDC Hamiltonian to include the transverse degrees of freedom

$$\hat{H}_{\mathrm{PDC}}(t) \propto \chi^{(2)} \int_{\mathrm{V}} \mathrm{d}^3 r \, \hat{E}_{\mathrm{p}}^{(+)}(\mathbf{r},t)\hat{E}_{\mathrm{s}}^{(-)}(\mathbf{r},t)\hat{E}_{\mathrm{t}}^{(-)}(\mathbf{r},t) + h.c. \qquad (11.58)$$

Following the presentation in [86], the boundary conditions imposed by the waveguide on the electric fields define a finite set of transverse-field distributions

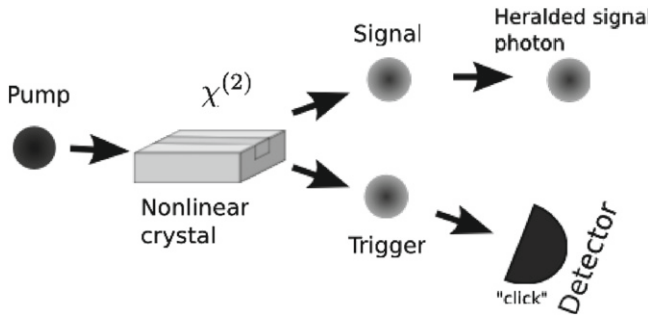

FIGURE 11.27 Single-photon generation using PDC in a nonlinear optical waveguide. The guiding structure gives rise to an enhanced down-conversion rate and a collinear propagation of all involved fields in well-defined spatial modes.

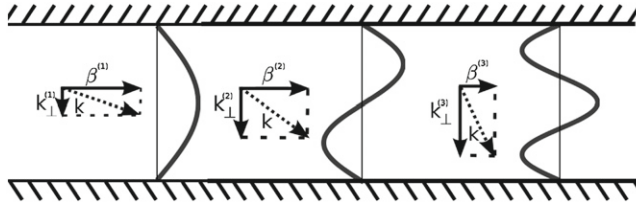

FIGURE 11.28 Schematic spatial modes and k-vectors of an electric field propagating inside a 1D waveguide.

$f^{(k)}(x,y)$ propagating inside the waveguide. This is sketched in Fig. 11.28 for a one-dimensional waveguide. The propagating field in a given spatial mode is defined by its **k**-vector, which is split into the $\beta^{(k)}$ component describing the propagation constant through the material, and $k_{\perp}^{(k)}$ related to the individual transverse-spatial-mode distribution $f^{(k)}(x,y)$. This is in sharp contrast to down-conversion in bulk crystals. Instead of emitting the signal and trigger fields into a continuous set of spatial modes, the down-converted beams are generated in a finite set of well-defined spatial modes imposed not by the PDC process but by the waveguide parameters. The electric fields inside the channel are therefore of the form

$$\hat{E}_{\mathrm{x}}^{(+)} = \hat{E}_{\mathrm{x}}^{(-)\dagger} = A \sum_{\mathrm{k}} f_{\mathrm{x}}^{(k)}(x,y) \int \mathrm{d}\omega_{\mathrm{x}} \exp\left[i \left(\beta_{\mathrm{x}}^{(k)}(\omega_{\mathrm{x}}) z - \omega_{\mathrm{x}} t \right) \right] \hat{a}_{\mathrm{x}}^{(k)}(\omega_{\mathrm{x}}). \tag{11.59}$$

In Eq. (11.59), A collects all constants, the x subscript labels the signal, trigger, or pump field, and the superscript (k) labels the spatial mode. Note that both the spatial field distribution $f_{\mathrm{x}}^{(k)}(x,y)$ and the effective k-vector $\beta_{\mathrm{x}}^{(k)}$ are dissimilar for the signal, trigger, and pump fields due to varying wavelengths and polarizations, which impact the spatial-mode distributions. In Eq. (11.59) we assume fields which are not too broad in frequency, $\Delta\omega \ll \omega_{\mathrm{c}}$, which means we may neglect the frequency dependence in the spatial distribution function about the central wavelength. Again, we treat the strong pump field as a classical wave, which yields the formula

$$E_{\mathrm{p}}^{(+)} = E_{\mathrm{p}}^{(-)*} = A \sum_{\mathrm{k}} f_{\mathrm{p}}^{(k)}(x,y) \int \mathrm{d}\omega_{\mathrm{p}}\, \alpha(\omega_{\mathrm{p}}) \exp\left[\imath \left(\beta_{\mathrm{p}}^{(k)}(\omega_{\mathrm{p}}) z - \omega_{\mathrm{p}} t \right) \right]. \tag{11.60}$$

We use Eqs. (11.18), (11.58),(11.59), and (11.60) to calculate the two-photon output state. By incorporating the three-dimensional structure of all involved fields we finally arrive at the following formula

$$\int_{t_0}^{t} \mathrm{d}t'\, \hat{H}_{\mathrm{PDC}}(t') = B \int_{t_0}^{t} \mathrm{d}t' \sum_{\mathrm{klm}} \underbrace{\iint \mathrm{d}x\,\mathrm{d}y\, f_{\mathrm{p}}^{(k)}(x,y)\, f_{\mathrm{s}}^{(l)}(x,y)\, f_{\mathrm{t}}^{(m)}(x,y)}_{A_{\mathrm{klm}}}$$
$$\times \int_{-\frac{L}{2}}^{\frac{L}{2}} \mathrm{d}z \iiint \mathrm{d}\omega_{\mathrm{p}}\mathrm{d}\omega_{\mathrm{s}}\mathrm{d}\omega_{\mathrm{t}}\, \alpha(\omega_{\mathrm{p}})$$
$$\times \exp\left[-i\left(\omega_{\mathrm{p}} - \omega_{\mathrm{s}} - \omega_{\mathrm{t}}\right) t'\right]$$
$$\times \exp\left[i\left(\beta_{\mathrm{p}}^{(k)}(\omega_{\mathrm{p}}) - \beta_{\mathrm{s}}^{(l)}(\omega_{\mathrm{s}}) - \beta_{\mathrm{t}}^{(m)}(\omega_{\mathrm{t}})\right) z\right]$$
$$\times \hat{a}_{\mathrm{s}}^{(l)\dagger}(\omega_{\mathrm{s}})\hat{a}_{\mathrm{t}}^{(m)\dagger}(\omega_{\mathrm{t}}) + h.c..$$
(11.61)

Equation (11.61) is very similar to Eq. (11.19) in Section 11.2 neglecting the transverse degree of freedom and describing a collinear interaction. Following the discussion in Section 11.2, we are able to calculate the generated waveguided PDC state as

$$\begin{aligned}
|\psi\rangle_{\mathrm{PDC}} &= |0\rangle + B' \sum_{\mathrm{klm}} A_{\mathrm{klm}} \iint \mathrm{d}\omega_{\mathrm{s}}\mathrm{d}\omega_{\mathrm{t}}\, \alpha(\omega_{\mathrm{s}} + \omega_{\mathrm{t}}) \\
&\quad \times \mathrm{sinc}\left[\Delta\beta_{\mathrm{klm}}\left(\omega_{\mathrm{s}},\omega_{\mathrm{t}}\right)\frac{L}{2}\right] \hat{a}_{\mathrm{s}}^{(l)\dagger}(\omega_{\mathrm{s}})\hat{a}_{\mathrm{t}}^{(m)\dagger}(\omega_{\mathrm{t}})\,|0\rangle \\
&= |0\rangle + B' \sum_{\mathrm{klm}} A_{\mathrm{klm}} \iint \mathrm{d}\omega_{\mathrm{s}}\mathrm{d}\omega_{\mathrm{t}}\, \alpha(\omega_{\mathrm{s}} + \omega_{\mathrm{t}}) \\
&\quad \times \Phi_{\mathrm{klm}}(\omega_{\mathrm{s}},\omega_{\mathrm{t}})\hat{a}_{\mathrm{s}}^{(l)\dagger}(\omega_{\mathrm{s}})\hat{a}_{\mathrm{t}}^{(m)\dagger}(\omega_{\mathrm{t}})\,|0\rangle \\
&= |0\rangle + B' \sum_{\mathrm{klm}} A_{\mathrm{klm}} \iint \mathrm{d}\omega_{\mathrm{s}}\mathrm{d}\omega_{\mathrm{t}}\, f_{\mathrm{klm}}(\omega_{\mathrm{s}},\omega_{\mathrm{t}})\hat{a}_{\mathrm{s}}^{(l)\dagger}(\omega_{\mathrm{s}})\hat{a}_{\mathrm{t}}^{(m)\dagger}(\omega_{\mathrm{t}})\,|0\rangle\,,
\end{aligned}$$
(11.62)

where all constants have been merged into B'.

The main modification with respect to the simplified model is the appearance of the overlap integral over the three interacting spatial modes, which introduces the coupling constant

$$A_{\mathrm{klm}} = \iint \mathrm{d}x\mathrm{d}y\, f_{\mathrm{p}}^{(k)}(x,y)\, f_{\mathrm{s}}^{(l)}(x,y)\, f_{\mathrm{t}}^{(m)}(x,y). \tag{11.63}$$

Hence the efficiency of the down-conversion becomes dependent on the spatial shape of the interacting spatial-mode triplet. If the pump, signal, and trigger propagate in similar modes an output state will be generated with high efficiency, but if the signal and trigger modes are sufficiently distinct the photon-pair generation efficiency will be strongly diminished. In addition, the phase-matching

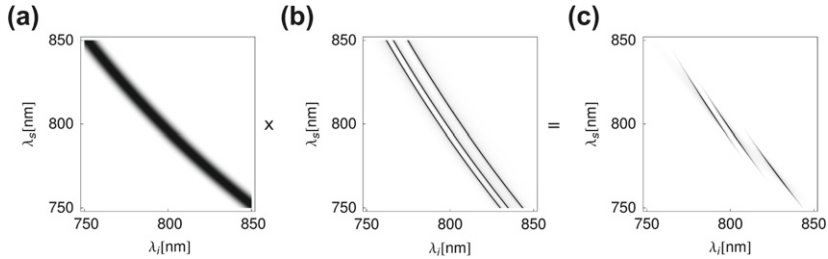

FIGURE 11.29 Sketch of the frequency distribution generated by a spectrally multimode PDC process [86]. (a) Pump distribution $\alpha(\omega_s + \omega_t)$, (b) phase-matching function $\Phi_{klm}(\omega_s,\omega_t)$ for the interacting mode triplets, (c) joint-spectral distribution function $f_{klm}(\omega_s,\omega_t)$. Each triplet of interacting modes exhibits a distinct spectral shape.

function $\Phi_{klm}(\omega_s,\omega_t)$ is now dependent on the spatial modes inside the waveguide, as each interacting mode triplet features a distinct β-vector mismatch

$$\Delta\beta^{(klm)}(\omega_p, \omega_s, \omega_t) = \beta_p^{(k)}(\omega_p) - \beta_s^{(l)}(\omega_s) - \beta_t^{(m)}(\omega_t). \tag{11.64}$$

Different spatial modes lead to a modification of the propagation vectors β_i, which consequently translates the phase-matching function in frequency space. This creates an individual phase-matching function for each interacting spatial-mode triplet, and in effect a different joint-spectral amplitude.

Figure 11.29 sketches, the pump distribution, the multitude of phase-matching functions, and the three distinct spectral shapes generated by the source presented in [86].

Direct measurements of the spatial- and spectral-mode structure in waveguided PDC are presented in [86,106,107]. Figure 11.30 shows the measured spectral distributions of the signal and trigger photons (labeled idler in this picture) of the waveguided KTP down-conversion source presented in [106]. Each peak, labeled A–E corresponds to different spatial-mode triplets (signal, trigger, and pump) propagating inside the material. By measuring the spatial-mode distribution of each peak one can resolve the different spatial modes of the signal and trigger beams, ranging from simple Gaussian distributions to more complicated higher-order structures (see Fig. (11.31)). Details are presented in [106].

Employing waveguides for PDC processes offers several advantages over bulk-PDC sources. It enables control of generated spatial distributions by engineering the design of the waveguiding structure. Whereas bulk PDC emits photon pairs into a large set of spatial modes at different angles, waveguided PDC restricts the two-photon states to well-defined spatial modes ideally suited for high collection efficiencies and coupling into optical fibers. Furthermore the confinement of PDC inside a waveguide leads to an increased overlap of the involved fields A_{klm} and to the restriction of the interaction couplings to

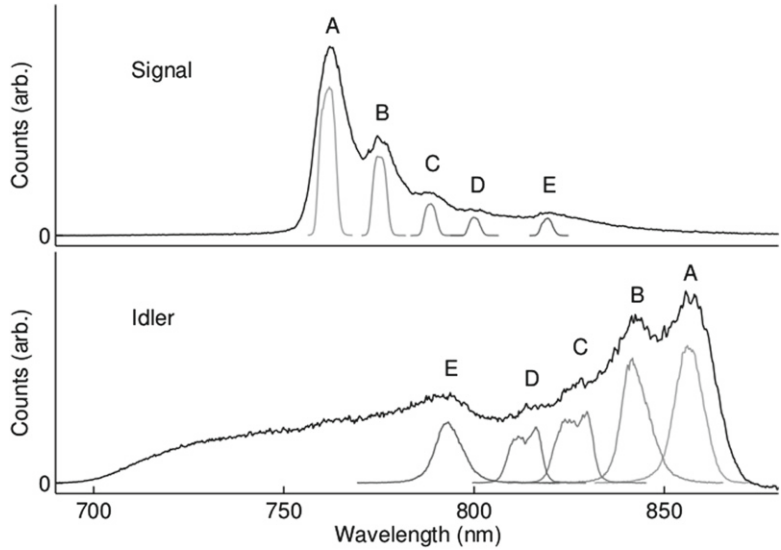

FIGURE 11.30 Spectral distribution of spatial multimode PDC in a nonlinear KTP waveguide [106] (Idler ≡ Trigger). The different peaks A-E stem from distinct interacting pump, signal, and trigger spatial-mode triplets inside the waveguide.

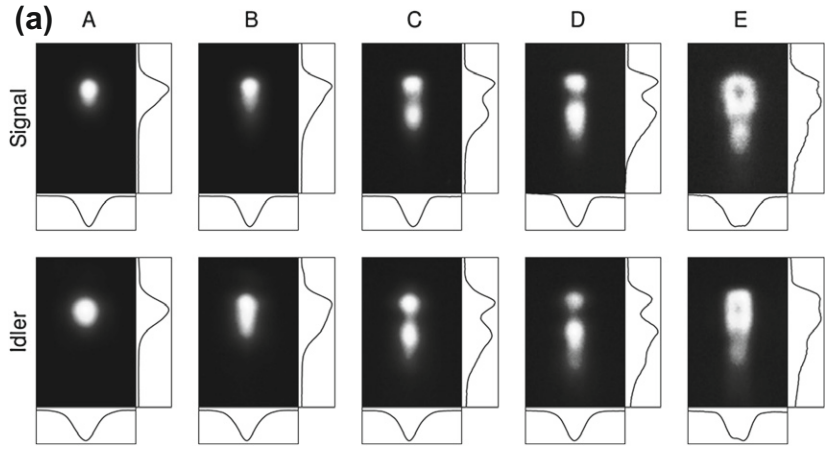

FIGURE 11.31 Spatial mode distribution of the different spectral PDC distributions presented in [106](Idler ≡ Trigger).

a discrete number of modes. This in turn significantly boosts the photon-pair generation probability [108, 109]. Finally, the interaction of the three fields is strictly collinear, and this greatly eases the experimental alignment and

post-processing of the beams in the laboratory. It should however be noted that waveguides feature a slightly enhanced loss rate in comparison to the surrounding bulk material, which stem from additional scattering losses in the waveguide.

11.5.3 Heralding Single Photons from PDC in Waveguides

If we take into account the spatial degree of freedom for the heralding of single-photon states from waveguided PDC, the heralded signal assumes the form

$$\begin{aligned}\rho_{\mathrm{s}} &= \sum_{\mathrm{l},\mathrm{l}'} \iint \mathrm{d}\omega_{\mathrm{s}}\, \mathrm{d}\omega_{\mathrm{s}'} \left[\int \mathrm{d}\omega_{\mathrm{t}} \sum_{\mathrm{k},\mathrm{k}',m} f_{\mathrm{klm}}(\omega_{\mathrm{s}},\omega_{\mathrm{t}})\, f^{*}_{\mathrm{k}'\mathrm{l}'\mathrm{m}}(\omega_{\mathrm{s}'},\omega_{\mathrm{t}'}) \right] |\omega_{\mathrm{s}},l\rangle \langle \omega_{\mathrm{s}'},l'| \\ &= \sum_{\mathrm{l},\mathrm{l}'} \iint \mathrm{d}\omega_{\mathrm{s}}\, \mathrm{d}\omega_{\mathrm{s}'}\, j_{\mathrm{l},\mathrm{l}'}(\omega_{\mathrm{s}},\omega_{\mathrm{s}'})\, |\omega_{\mathrm{s}},l\rangle \langle \omega_{\mathrm{s}'},l'| \,, \end{aligned} \tag{11.65}$$

where $\omega_{\mathrm{s}},\omega_{\mathrm{s}'}$ label the frequencies of the heralded signal and l, l' its spatial mode. Hence the heralded single-photon states are, in general, prepared in a mixture of different frequencies and spatial modes. Of course this is a highly detrimental effect for the heralding of pure single-photon Fock states. In order to achieve a high purity for the single-photon Fock-state generation we must not only consider the frequency degree of freedom as discussed in Section 11.2.4, but we must also consider the spatial degree of freedom.

In Section 11.2.3 we learned how to cope with mixing effects that stem from frequency correlations. In fact, the impact of the spatial degree of freedom on the heralding of single photons is mathematically almost identical to the spectral degree of freedom. As in the frequency domain, the easiest and most straightforward approach is to apply filtering, for example employing small pinholes or single-mode fibers to purify the trigger photon, which results in the propagation of spatially pure signal states. This, however, greatly reduces the heralding efficiency because a large fraction of the beam is lost.

To study the impact of the spatial modes on the heralded signal in more detail we start by neglecting the frequency properties of the state in Eq. (11.65) and assume monochromatic signal and trigger modes. The heralded signal is transformed to

$$\rho_{\mathrm{s}} = \sum_{\mathrm{k},\mathrm{l}} \sum_{\mathrm{k}',\mathrm{l}'} \sum_{\mathrm{m}} f_{\mathrm{klm}} f^{*}_{\mathrm{k}'\mathrm{l}'\mathrm{m}}\, |l\rangle \langle l'| \,, \tag{11.66}$$

where (k, k') labels the spatial modes of the pump beam, (l, l') the modes of the signal beam and m the trigger modes. From Eq. (11.66) it is evident that the heralded signal photon is, in general, in a mixture of spatial modes, and consequently not in a pure single-photon Fock state.

One method to herald single-spatial-mode single photons is to create the PDC state in only a single trigger mode m, which leads to the heralding of a

spatially pure signal photon

$$\begin{aligned}\rho_\mathrm{s} &= \sum_{\mathrm{k,l}} \sum_{\mathrm{k',l'}} f_\mathrm{klm} f^*_\mathrm{k'l'm} \left|l\right\rangle \left\langle l'\right| \\ &= \sum_{\mathrm{k,l}} f_\mathrm{klm} \left|l\right\rangle \sum_{\mathrm{k',l'}} f^*_\mathrm{k'l'm} \left\langle l'\right| \\ &= \left|\psi_\mathrm{s}\right\rangle \left\langle\psi_\mathrm{s}\right| . \end{aligned} \tag{11.67}$$

Alternatively it is also sufficient to engineer the signal emission into a single mode. In this case the heralded state becomes

$$\rho_\mathrm{s} = \underbrace{\sum_{\mathrm{k}} \sum_{\mathrm{k'}} \sum_{\mathrm{m}} f_\mathrm{klm} f^*_\mathrm{k'lm}}_{\mathrm{d}} \left|l\right\rangle \left\langle l\right| = d \left|l\right\rangle \left\langle l\right| = \left|\psi_\mathrm{s}\right\rangle \left\langle\psi_\mathrm{s}\right| . \tag{11.68}$$

Engineering single-spatial-mode behavior in a waveguide is an elegant method to cope with spatial-mode effects. If the guiding structure is designed to allow only single-mode propagation of the signal or trigger photon, the heralded state will be pure in this domain and no spatial mixing occurs. This can be achieved by a custom waveguide design where the diameters of the guide geometry are adapted to the signal or trigger field. Note, however, that the pump beam, which has a shorter wavelength then the signal and trigger, might still be able to propagate in a higher spatial mode. This can distort the frequency shape of the heralded photons, as different modes typically also exhibit different spectral properties (see Section 11.5.3). However, this effect can be mediated by a careful coupling of the pump wave into the fundamental waveguide mode.

In between the two extremes of strong filtering and careful engineering of the spatio-spectral structure of PDC there exists a third method to eliminate all but one interacting spatial-mode triplet. Introducing spectral windowing we can exploit the fact that each down-conversion process features a distinct joint-spectral amplitude distribution $f_\mathrm{klm}(\omega_\mathrm{s}, \omega_\mathrm{t})$, for each spatial-mode triplet, as depicted in Fig. 11.29, which is caused by the unique β-vector mismatch between the three interacting beams. Using this characteristic it is possible to spatially purify the down-conversion by placing broadband (and thus low loss) spectral filters in the signal and trigger arm that transmit only one process $f_\mathrm{klm}(\omega_\mathrm{s},\omega_\mathrm{t})$. Hence we can eliminate the spatial multimode effects without introducing losses to the targeted down-conversion process. Still, the applicability of this approach is closely related to the specific characteristics of the individual source. A more detailed review—featuring experimental data—is presented in [106].

In summary all three approaches lead to the same result. The considered PDC components become single mode in the spatial domain and consequently the heralded signal photon can be represented in the form of Eq. (11.24). The effects from the spatial domain are negated and efficient creation and heralding

of pure single-photon Fock states with well-defined spatial-mode profiles is possible.

11.5.4 Electric Field Modes in Waveguides

The main challenge when analyzing the exact spatial structure of PDC in waveguides is the theoretical modeling of the transverse-field distributions defined by the channel. As a first step one has to get access to the refractive-index profile of the waveguide. The easiest approach is to perform microscopy at the input or output facet to get a general impression of the structure, as shown in Fig. 11.26.

This measurement already provides some insight on the waveguide properties, and opens up a route to assess the width and height of the structure. However this approach does not give access to the refractive-index step Δn between the waveguide and the material, which must be estimated (common values are $\Delta n \approx 0.01$). More precise methods have been developed in the context of fabricating classical optical devices, for example M-line spectroscopy, and the inverse WKB method enabling precise access to the to refractive-index distribution of the waveguide [110].

For a given refractive-index distribution inside the waveguide there exist various methods to calculate the guided spatial modes, depending on the geometry of the system. Assuming rectangular or circular waveguides with perfectly conducting edges—the mathematical analog of modes inside an infinitely deep potential well ($\Delta n = \infty$)—is the most simplistic model and has the advantage of yielding an analytic solution. Including the effects of finite refractive-index steps Δn, a completely analytical solution is not possible, but a semi-analytical approach, is presented in [111], which relies on the solution of transcendental equations. As more complex waveguide geometries are considered, such as non-rectangular waveguide structures with slowly varying refractive indices Δn, full numerical theories must be utilized. Mode-solving techniques based on finite element approaches [112] are common, and various software applications are available for this purpose.

11.5.4.1 Analytic Waveguide Model

In this book we restrict ourselves to the discussion of the straightforward analytical model, which gives a fair introduction to the physics involved. In this model we assume a rectangular waveguide of width w and height h with perfectly conducting edges (i.e., the electric fields are zero at the boundaries).

To calculate the electric field propagation in three dimensions, we express the electric field as

$$\begin{aligned} \mathbf{E}(x,y,z) &= \left[\mathbf{e}_\mathrm{x} E_\mathrm{x}(x) + \mathbf{e}_\mathrm{y} E_\mathrm{y}(y) + \mathbf{e}_\mathrm{z} E_\mathrm{z}(z)\right] e^{-i\omega t} \\ E_\mathrm{i}(j) &= E_\mathrm{i} e^{ik_\mathrm{i} j}. \end{aligned} \tag{11.69}$$

Here we define z as the propagation direction of the beam, and the x and y components label the transverse degrees of freedom. The absolute value of the wave vector of a light ray inside a medium, propagating alongside a crystal axis i, is given by

$$|k|^2 = k_x^2 + k_y^2 + k_z^2 = \frac{\omega}{c} n_i(\omega) = \frac{2\pi}{\lambda} n_i(\lambda). \tag{11.70}$$

During the PDC process we are mostly interested in the momentum or wave-vector mismatch between the interacting fields in propagation direction, which we label β and that can be calculated by

$$\beta^2 = |k|^2 - k_x^2 - k_y^2 \tag{11.71}$$

The solutions for an electric field in a infinitely deep potential well are well known

$$\begin{aligned} E_x(x) &= \sin\left(\frac{\nu\pi}{w} x\right), \\ E_y(y) &= \sin\left(\frac{\mu\pi}{h} y\right), \end{aligned} \tag{11.72}$$

where ν and μ label the spatial mode of the standing-wave solution in the waveguide $\nu, \mu = \mathbb{N}^+ \backslash \{0\}$, with the corresponding k-vectors

$$\begin{aligned} k_x &= \frac{\nu\pi}{w}, \\ k_y &= \frac{\mu\pi}{w}. \end{aligned} \tag{11.73}$$

Using Eq. (11.73) we arrive at the effective propagating wave vector:

$$\beta^2(\lambda) = \left(\frac{2\pi}{\lambda} n_x(\lambda)\right)^2 - \left(\frac{\nu\pi}{w}\right)^2 - \left(\frac{\mu\pi}{h}\right)^2 \tag{11.74}$$

For practical purposes it is more elegant to write this effective k-vector β in the propagation direction as an effective Sellmeier equation

$$n_{\text{eff}}^2(\lambda) = n_x^2(\lambda) - \left(\frac{\lambda\nu}{2w}\right) - \left(\frac{\lambda\mu}{2h}\right). \tag{11.75}$$

Despite the simplicity of this model, it yields quite accurate values for the generated mode distributions and effective k-vectors inside the waveguide, given only the width and height of the system. It is very useful to obtain a qualitative simulation of the process, however, when precise quantitative predictions are required, the semi-analytic approach by Marcuse [111] or finite element methods [112] should be applied.

11.6 COMPARISON OF EXPERIMENTAL SINGLE-PHOTON SOURCES USING PDC

Type	Reference	Crystal	Heralding efficiency	Heralding rate c/s	Wavelength (Bandwidth)	Special remarks
Bulk	Mosley 2008 [43]	KDP	44%	150	t=830 (20), s=830 (3.5)	spectral purity 0.95
Periodically-poled	Ljunggren 2005 [63]	ppKTP	48%	7,200	t=810 (2) s=1550	cw-pumped, SMF-coupling, $g^{(2)}(0)=0.024$
	Castelletto 2006 [64]	ppLN	48%	-	t=810 (2) s=1550	cw-pumped, SMF-coupling, different focusing conditions
	Fedrizzi 2007 [65]	ppKTP	22%	53,000	t=810 s=810	cw-pumped, study of different focusing conditions
	Scholz 2009 [75]	ppKTP	55%	5,000	t= - (3MHz) s= - (3MHz)	in cavity, $g^{(2)}(0)=0.01$
	Bocquillon 2009 [72]	ppKTP	30%	80,000	t=810 s=810	pulsed pump, $g^{(2)}(0)=0.08$
	Evans 2010 [79]	ppKTP	19.0%	1000	t=1552 (1) s=1552 (1)	SMF-coupling, spectral Schmidt number 1.07
	Smith 2012 [69]	ppKTP	80%	~10,000	t=820 (3) s=820	cw-pumped, SMF-coupling, TES detectors
	Brida 2012 [77]	ppKTP	-	~ 5	t=810 (10) s=1550 (30)	$g^{(2)}(0)=0.005$, optical shutter to supress background
	Pereira 2013 [68]	ppKTP	84%	11,000	t=810 (0.2) s=810 (0.2)	cw-pumped, SMF-coupling, symmetric heralding efficiency
	Ramelow 2013 [70]	ppKTP	87%	5,500	t=810 (0.5) s=810 (0.5)	TES detectors
Waveguide	Tanzilli 2001 [93]	ppLN	-	1,500	s=1314 (30)	first experiment in waveguides
	U'Ren 2004 [95]	ppKTP	85%	1,270	s=800	-
	Zhong 2010 [98]	ppKTP	-	3,000	s=1316 (1.2)	-
	Eckstein 2011[100]	ppKTP	60%	-	~1550 (5)	$g^{(2)}(0)=0.05$, Spectral purity=0.8/0.95 (Raw / background correction), mean photon number: 2.5
	Krapick 2013 [97]	ppLN	60%	105	t=803 (0.7) s=1575	$g^{(2)}(0)$ =0.004
	Harder 2013 [102]	ppKTP	80%	-	t=1535 (4) s=1535 (4)	mean photon number: up to 80, spectral purity = 0.86 (raw)

FIGURE 11.32 Overview of selected experimental realisations of heralded single-photon sources using PDC. The table is divided into bulk, periodically-poled and waveguide parts, the references are ordered chronologically, and the name of the nonlinear crystal used is given. The heralding efficiency includes optical loses but no detection efficiencies. The heralding rate is the absolute rate measured, i.e., the raw coincidence rate. The central wavelength of the trigger and signal photons is given with their respective bandwidths in brackets. Additional experimental details and measurements on photon-number purity and spectral purity are summarized under remarks.

11.7 OVERVIEW OF THE MOST COMMONLY USED NONLINEAR MATERIALS AND THEIR PROPERTIES

Crystal	Quasi phase-matching	Waveguide	Nonlinearity	Phase-matching	Damage threshold	Transparency range (nm)
BBO	-	Yes	d_{24} = 0.13 pm/V d_{22} = 2.6 pm/V	Type-II Type-0	5 GW/cm^2	189 - 3500
LBO	-	Yes	d_{24} = -0.67 pm/V	Type-II	9.5 GW/cm^2	160 - 2600
LN	Yes	Yes	d_{33} = 27.0 pm/V	Type-0	0.2 GW/cm^2	420 - 5200
KTP	Yes	Yes	d_{33} = 16.9 pm/V d_{24} = 7.6 pm/V	Type-0 Type-II	2.5 GW/cm^2	350- 4500
BIBO	-	Yes	d_{11} = 2.5 pm/V	Type-I	0.3 GW/cm^2	286 - 2500
KNbO3	Yes	Yes	d_{32} = -18.3 pm/V	Type-I	0.4 MW/cm^2	400 - 4500
AlGaAs	Yes	Yes	d_{14}=100 pm/V	Type-II	-	> 1000

FIGURE 11.33 Overview of commonly used nonlinear materials for production of heralded single photons. Quasi-phase-matching and waveguide indicate if these modifications are available for the specific material. Strength of $\chi^{(2)}$-nonlinearities is given together with the type of possible phase-matching (only the most common types are listed). Damage thresholds indicate the maximum intensity for the pump laser. Transparency data list the range over which the material is transparent. Note that nonlinearities and damage thresholds are wavelength dependent. Therefore, the values quoted here should only be taken as approximate.

11.8 CONCLUSION

In conclusion, parametric down-conversion is a mature technology for single-photon sources. The spectral and spatio-temporal profiles of PDC light are extremely well understood and can be tailored to meet the demands of modern applications. Advances in nonlinear optics have made PDC sources very efficient and well suited for on-chip integration, which becomes increasingly important as quantum technology moves from laboratories to real-world applications.

The remaining challenge is to combine the theoretic and engineering advances presented in this chapter into one package that delivers pure heralded single photons on demand. The probabilistic nature of the PDC process is acceptable for some applications, such as quantum key distribution, but less so for others, such as quantum logic gates or quantum metrology. A solution may be provided by combining PDC sources with novel nonlinear techniques such as strong two-photon absorbers similar to the scheme shown in [113], for which several systems are studied. Until such schemes become available, PDC sources can approximate single photons to virtually any desired degree by using multiplexing techniques that necessitate a modest engineering overhead once sources, logic gates, and detectors are all integrated on a single photonic chip.

REFERENCES

[1] D. Magde and H. Mahr, "Study in Ammonium Dihydrogen Phosphate of Spontaneous Parametric Interaction Tunable from 4400 to 16 000 Å," Phys. Rev. Lett. 18, 905–907 (1967).

[2] S.A. Akhmanov, V.V. Fadeev, R.V. Khoklov, and O.N. Chunaev, Sov. Phys. JETP Lett. 6, 85 (1967).
[3] R.L. Byer and S.E. Harris, "Power and Bandwidth of Spontaneous Parametric Emission," Phys. Rev. 168, 1064 (1968).
[4] D.C. Burnham and D.L. Weinberg, "Observation of Simultaneity in Parametric Production of Optical Photon Pairs," Phys. Rev. Lett. 25, 84–87 (1970).
[5] Y.H. Shih and C.O. Alley, "New Type of Einstein-Podolsky-Rosen-Bohm Experiment Using Pairs of Light Quanta Produced by Optical Parametric Down Conversion," Phys. Rev. Lett. 61, 2921–2924 (1988).
[6] R. Ghosh and L. Mandel, "Observation of Nonclassical Effects in the Interference of Two Photons," Phys. Rev. Lett. 59, 1903–1905 (1987).
[7] C.K. Hong, Z.Y. Ou, and L. Mandel, "Measurement of Subpicosecond Time Intervals Between Two Photons by Interference," Phys. Rev. Lett. 59, 2044–2046 (1987).
[8] P.G. Kwiat, K. Mattle, H. Weinfurter, A. Zeilinger, A.V. Sergienko, and Y. Shih, "New High-Intensity Source of Polarization-Entangled Photon Pairs," Phys. Rev. Lett. 75, 4337–4341 (1995).
[9] G. Weihs, T. Jennewein, C. Simon, H. Weinfurter, and A. Zeilinger, "Violation of Bell's Inequality Under Strict Einstein Locality Conditions," Phys. Rev. Lett. 81, 5039–5043 (1998).
[10] D. Bouwmeester, J.W. Pan, K. Mattle, M. Eibl, H. Weinfurter, and A. Zeilinger, "Experimental Quantum Teleportation," Nature 390, 575–579 (1997).
[11] D. Bouwmeester, J.W. Pan, M. Daniell, H. Weinfurter, and A. Zeilinger, "Observation of Three-Photon Greenberger-Horne-Zeilinger Entanglement," Phys. Rev. Lett. 82, 1345–1349 (1999).
[12] T. Jennewein, C. Simon, G. Weihs, H. Weinfurter, and A. Zeilinger, "Quantum Cryptography with Entangled Photons," Phys. Rev. Lett. 84, 4729–4732 (2000).
[13] R.W. Boyd, Nonlinear Optics Second Edition, Academic Press (2003).
[14] T. Suhara and M. Fujimura, Waveguide Nonlinear-Optic Devices (Springer Series in Photonics, V. 11). SpringerVerlag (2003).
[15] W.P. Grice and I.A. Walmsley, "Spectral Information and Distinguishability in Type-II Down-Conversion with a Broadband Pump," Phys. Rev. A 56, 1627 (1997).
[16] W. Wasilewski, C. Radzewicz, R. Frankowski, and K. Banaszek, "Statistics of Multiphoton Events in Spontaneous Parametric Down-Conversion," Phys. Rev. A 78, 033831 (2008).
[17] W. Mauerer, M. Avenhaus, W. Helwig, and C. Silberhorn, "How Colors Influence Numbers: Photon Statistics of Parametric Down-Conversion," Phys. Rev. A 80, 053815 (2009).
[18] K.N. Cassemiro, K. Laiho, and C. Silberhorn, "Accessing the Purity of a Single Photon by the Width of the Hong–Ou–Mandel Interference," New J. Phys. 12, 113052 (2010).
[19] W. Wasilewski, P. Kolenderski, and R. Frankowski, "Spectral Density Matrix of a Single Photon Measured," Phys. Rev. Lett. 99, 123601 (2007).
[20] C.K. Law, I.A. Walmsley, and J.H. Eberly, "Continuous Frequency Entanglement: Effective Finite Hilbert Space and Entropy Control." Phys. Rev. Lett. 84, 5304–5307 (2000).
[21] P.P. Rohde, W. Mauerer, and C. Silberhorn, "Spectral Structure and Decompositions of Optical States, and Their Applications," New J. Phys. 9, 91 (2007).
[22] J.H. Eberly, "Schmidt Analysis of Pure-State Entanglement," Laser Phys. 16, 921–926 (2006).
[23] G. Vidal and R.F. Werner, "Computable Measure of Entanglement," Phys. Rev. A 65, 032314 (2002).
[24] A.M. Brańczyk, T. C. Ralph, W. Helwig, and C. Silberhorn, "Optimized Generation of Heralded Fock States Using Parametric Down-Conversion," New J. Phys. 12, 063001 (2010).
[25] K. Laiho, K.N. Cassemiro, and C. Silberhorn, "Producing High Fidelity Single Photons with Optimal Brightness Via Waveguided Parametric Down-Conversion," Opt. Express 17, 22823–22837 (2009).

[26] A.B. U'Ren, C. Silberhorn, R. Erdmann, K. Banaszek, W.P. Grice, I.A. Walmsley, and M.G. Raymer, "Generation of Pure-State Single-Photon Wavepackets by Conditional Preparation Based on Spontaneous Parametric Downconversion." Laser Phys. 15, 146–161 (2005).
[27] A. Christ, A. Eckstein, P.J. Mosley, and C. Silberhorn, "Pure Single Photon Generation by Type-I PDC with Backward-Wave Amplification," Opt. Express 17, 3441–3446 (2009).
[28] S.L. Braunstein and P. van Loock, "Quantum Information with Continuous Variables," Rev. Mod. Phys. 77, 513–577 (2005).
[29] P. Kok and S.L. Braunstein, "Postselected Versus Nonpostselected Quantum Teleportation Using Parametric Down-Conversion," Phys. Rev. A 61, 042304 (2000).
[30] P. Kok, W.J. Munro, K. Nemoto, T.C. Ralph, J.P. Dowling, and G.J. Milburn, "Review Article: Linear Optical Quantum Computing," Rev. Mod. Phys. 79, 135 (2007).
[31] H. Lee, U. Yurtsever, P. Kok, G.M. Hockney, C. Adami, S.L. Braunstein, and J.P. Dowling, "Towards Photostatistics from Photon-Number Discriminating Detectors," J. Mod. Opt. 51, 1517–1528 (2004).
[32] P. Kumar, P. Kwiat, A. Migdall, S.W. Nam, J. Vuckovic, and F.N.C. Wong, "Photonic Technologies for Quantum Information Processing," Quantum Inf. Process. 3, 215–231 (2004).
[33] N.A. Peters, K.J. Arnold, A.P. VanDevender, E.R. Jeffrey, R. Rangarajan, O. Hosten, J.T. Barreiro, J.B. Altepeter, and P.G. Kwiat, "Towards a Quasi-Deterministic Single-Photon Source," SPIE 6305, 630507 (2006).
[34] X. Ma, S. Zotter, J. Kofler, T. Jennewein, and A. Zeilinger, "Experimental Generation of Single Photons Via Active Multiplexing," Phys. Rev. A 83, 04 (2011).
[35] V.G. Dmitriev, G.G. Gurzadyan, and D.N. Nikogosyan, Handbook of Nonlinear Optical Crystals, volume 64. Springer, Berlin and New York (1999).
[36] SNLO website. *http://www.as-photonics.com/SNLO.html*.
[37] R. Rangarajan, M. Goggin, and P. Kwiat, "Optimizing Type-I Polarization-Entangled Photons," Opt. Express 17, 18920–18933 (2009).
[38] A. Halevy, E. Megidish, L. Dovrat, H.S. Eisenberg, P. Becker, and L. Bohatý, "The Biaxial Nonlinear Crystal BiB_3O_6 as a Polarization Entangled Photon Source Using Non-Collinear Type-II Parametric Down-Conversion," Opt. Express 19, 20420–20434 (2011).
[39] C. Kurtsiefer, M. Oberparleiter, and H. Weinfurter, "High-Efficiency Entangled Photon Pair Collection in Type-II Parametric Fluorescence," Phys. Rev. A 64, 023802 (2001).
[40] F.A. Bovino, P. Varisco, A.M. Colla, G. Castagnoli, G. Di Giuseppe, and A.V. Sergienko, "Effective Fiber-Coupling of Entangled Photons for Quantum Communication," Opt. Commun. 227, 343–348 (2003).
[41] S. Castelletto, I.P. Degiovanni, A. Migdall, and M. Ware, "On the Measurement of Two-Photon Single-Mode Coupling Efficiency in Parametric Down-Conversion Photon Sources," New J. Phys. 6, 87 (2004).
[42] P. Kolenderski, W. Wasilewski, and K. Banaszek, "Modeling and Optimization of Photon Pair Sources Based on Spontaneous Parametric Down-Conversion," Phys. Rev. A 80, 013811 (2009).
[43] P.J. Mosley, J.S. Lundeen, B.J. Smith, P. Wasylczyk, A.B. U'Ren, C. Silberhorn, and I.A. Walmsley, "Heralded Generation of Ultrafast Single Photons in Pure Quantum States," Phys. Rev. Lett. 100, 133601–133604 (2008).
[44] P.J. Mosley, J.S. Lundeen, B.J. Smith, and I.A. Walmsley, "Conditional Preparation of Single Photons Using Parametric Downconversion: A Recipe for Purity," New J. Phys. 10, 093011 (2008).
[45] A.M. Brańczyk, A. Fedrizzi, T.M. Stace, T.C. Ralph, and A.G. White, "Engineered Optical Nonlinearity for Quantum Light Sources," Opt. Express 19, 55–65 (2011).
[46] T. Jennewein, M. Barbieri, and A.G. White, "Single-Photon Device Requirements for Operating Linear Optics Quantum Computing Outside the Post-Selection Basis," J. Mod. Opt. 58, 276–287 (2011).
[47] A.L. Migdall, D. Branning, and S. Castelletto, "Tailoring Single-Photon and Multiphoton Probabilities of a Single-Photon On-Demand Source," Phys. Rev. A 66, 11 (2002).
[48] M.A. Broome, M.P. Almeida, A. Fedrizzi, and A.G. White, "Reducing Multi-Photon in Pulsed Down-Conversion by Temporal Multiplexing," Opt. Express 19, 22698–22708 (2011).

[49] G. Brida, I.P. Degiovanni, M. Genovese, A. Migdall, F. Piacentini, S.V. Polyakov, and I. Ruo Berchera, "Experimental Realization of a Low-Noise Heralded Single-Photon Source," Opt. Express 19, 1484–1492 (2011).
[50] J.A. Armstrong, N. Bloembergen, J. Ducuing, and P.S. Pershan, "Interactions Between Light Waves in a Nonlinear Dielectric," Phys. Rev. 127, 1918–1939 (1962).
[51] M.M. Fejer, G.A. Magel, D.H. Jundt, and R.L. Byer, "Quasi-Phase-Matched Second Harmonic-Generation: Tuning and Tolerances," IEEE J. Quantum Elect. 28, 2631–2654 (1992).
[52] K. Kato, and E. Takaoka, "Sellmeier and Thermo-Optic Dispersion Formulas for KTP," Appl. Opt. 41, 5040–5044 (2002).
[53] S. Emanueli, and A. Arie, "Temperature-Dependent Dispersion Equations for KTiOPO4 and KTiOAsO4," Appl. Opt. 42, 6661–6665 (2003).
[54] E.J. Lim, M.M. Fejer, and R.L. Byer, "Second-Harmonic Generation of Green Light in Periodically Poled Planar Lithium-Niobate Wave-Guide," Electron. Lett. 25, 174–175 (1989).
[55] C.J. van der Poel, J.D. Bierlein, J.B. Brown, and S. Colak, "Efficient Type-I Blue Second-Harmonic Generation in Periodically Segmented KTiOPO4 Waveguides," Appl. Phys. Lett. 57, 2074–2076 (1990).
[56] M. Yamada, N. Nada, M. Saitoh, and K. Watanabe, "First-Order Quasi-Phase Matched $LiNbO_3$ Wave-Guide Periodically Poled by Applying an External-Field for Efficient Blue Second-Harmonic Generation," Appl. Phys. Lett. 62, 435–436 (1993).
[57] M. Houe, and P.D. Townsend, "An Introduction to Methods of Periodic Poling for Second-Harmonic Generation," J. Phys. D – Appl. Phys. 28, 1747–1763 (1995).
[58] D.S. Hum, and M.M. Fejer, "Quasi-Phasematching," Comptes Rendus Physique 8, 180–198 (2007).
[59] E.J. Mason, M.A. Albota, F. Konig, and F.N.C. Wong, "Efficient Generation of Tunable Photon Pairs at 0.8 and 1.6 μm," Opt. Lett. 27, 2115–2117 (2002).
[60] C.E. Kuklewicz, M. Fiorentino, G. Messin, F.N.C. Wong, and J.H. Shapiro, "High-Flux Source of Polarization-Entangled Photons From a Periodically Poled KTiOPO4 Parametric Down-Converter," Phys. Rev. A 69, 013807 (2004).
[61] M. Fiorentino, G. Messin, C.E. Kuklewicz, F.N.C. Wong, and J.H. Shapiro, "Generation of Ultrabright Tunable Polarization Entanglement Without Spatial, Spectral, or Temporal Constraints," Phys. Rev. A 69, 041801 (2004).
[62] F. Konig, E.J. Mason, F.N.C. Wong, and M.A. Albota, "Efficient and Spectrally Bright Source of Polarization-Entangled Photons," Phys. Rev. A 71, 033805 (2005).
[63] D. Ljunggren, and M. Tengner, "Optimal Focusing for Maximal Collection of Entangled Narrow-Band Photon Pairs into Single-Mode Fibers," Pys. Rev. A 72, 062301 (2005).
[64] S. Castelletto, I.P. Degiovanni, V. Schettini, and A. Migdall, "Optimizing Single-Photon-Source Heralding Efficiency and Detection Efficiency Metrology at 1550 nm Using Periodically Poled Lithium Niobate," Metrologia 43, S56–S60 (2006).
[65] A. Fedrizzi, T. Herbst, A. Poppe, T. Jennewein, and A. Zeilinger, "A Wavelength-Tunable Fiber-Coupled Source of Narrowband Entangled Photons," Opt. Express 15, 15377–15386 (2007).
[66] R.S. Bennink, "Optimal Collinear Gaussian Beams for Spontaneous Parametric Down-Conversion," Phys. Rev. A 81, 053805 (2010).
[67] J.L. Smirr, M. Deconinck, R. Frey, I. Agha, E. Diamanti, and I. Zaquine, "Optimal Photon-Pair Single Mode Coupling in Narrow-Band Spontaneous Parametric Down-Conversion with Arbitrary Pump Profile," J. Opt. Soc. Am. B – Opt. Phys. 30, 288–301 (2013).
[68] M.D. Cunha Pereira, F.E. Becerra, B.L. Glebov, J. Fan, S.W. Nam, and A. Migdall, "Demonstrating Highly Symmetric Single-Mode, Single-Photon Heralding Efficiency in Spontaneous Parametric Downconversion," Opt. Lett. 38, 1609–1611 (2013).
[69] D.H. Smith, G. Gillett, M. de Almeida, C. Branciard, A. Fedrizzi, T.J. Weinhold, A. Lita, B. Calkins, T. Gerrits, S.W. Nam, and A.G. White, "Conclusive Quantum Steering with Superconducting Transition Edge Sensors," Nat. Commun. 3, 625 (2012).
[70] S. Ramelow, A. Mech, M. Giustina, S. Gröblacher, W. Wieczorek, J. Beyer, A. Lita, B. Calkins, T. Gerrits, S.W. Nam, A. Zeilinger, and R. Ursin, "Highly Efficient Heralding of Entangled Single Photons," Opt. Express 21, 6707–6717 (2013).

[71] B. Yurke, and M. Potasek, "Obtainment of Thermal Noise from a Pure Quantum State," Phys. Rev. A 36, 3464–3466 (1987).
[72] E. Bocquillon, C. Couteau, M. Razavi, R. Laflamme, and G. Weihs, "Coherence Measures for Heralded Single-Photon Sources," Phys. Rev. A 79, 035801 (2009).
[73] S. Fasel, O. Alibart, S. Tanzilli, P. Baldi, A. Beveratos, N. Gisin, and H. Zbinden, "High-Quality Asynchronous Heralded Single-Photon Source at Telecom Wavelength," New J. Phys. 6, 163 (2004).
[74] M. Tengner and D. Ljunggren, "Characterization of an Asynchronous Source of Heralded Single Photons Generated at a Wavelength of 1550 nm," arXiv:0706.2985v1, (2007).
[75] M. Scholz, L. Koch, and O. Benson, "Statistics of Narrow-Band Single Photons for Quantum Memories Generated by Ultrabright Cavity-Enhanced Parametric Down-Conversion," Phys. Rev. Lett. 102, 063603 (2009).
[76] D. Höckel, L. Koch, and O. Benson, "Direct Measurement of Heralded Single-Photon Statistics from a Parametric Down-Conversion Source," Phys. Rev. A 83, 013802 (2011).
[77] G. Brida, I.P. Degiovanni, M. Genovese, F. Piacentini, P. Traina, A. Della Frera, A. Tosi, A. Bahgat Shehata, C. Scarcella, A. Gulinatti, M. Ghioni, S.V. Polyakov, A. Migdall, and A. Guidice, "An Extremely Low-Noise Heralded Single-Photon Source: A Breakthrough for Quantum Technologies." App. Phys. Lett. 101, 221112 (2012).
[78] W.P. Grice, A.B. U'Ren, and I.A. Walmsley, "Eliminating Frequency and Space-Time Correlations in Multiphoton States," Phys. Rev. A 64, 063815 (2001).
[79] P.G. Evans, R.S. Bennink, W.P. Grice, T.S. Humble, and J. Schaake, "Bright Source of Spectrally Uncorrelated Polarization-Entangled Photons with Nearly Single-Mode Emission," Phys. Rev. Lett. 105, 253601 (2010).
[80] R.-B. Jin, J. Zhang, R. Shimizu, N. Matsuda, Y. Mitsumori, H. Kosaka, and K. Edamatsu, "High-Visibility Nonclassical Interference Between Intrinsically Pure Heralded Single Photons and Photons from a Weak Coherent Field," Phys. Rev. A 83, 031805 (2011).
[81] J.P. Torres, A. Alexandrescu, S. Carrasco, and L. Torner, "Quasi-Phase-Matching Engineering for Spatial Control of Entangled Two-Photon States," Opt. Lett. 29, 376–378 (2004).
[82] H.Y. Leng, X.Q. Yu, Y.X. Gong, P. Xu, Z.D. Xie, H. Jin, C. Zhang, and S.N. Zhu, "On-Chip Steering of Entangled Photons in Nonlinear Photonic Crystals," Nat. Commun. 2, 429 (2011).
[83] M.B. Nasr, S. Carrasco, B.E.A. Saleh, A.V. Sergienko, M.C. Teich, J.P. Torres, L. Torner, D.S. Hum, and M.M. Fejer, "Ultrabroadband Biphotons Generated Via Chirped Quasi-Phase-Matched Optical Parametric Down-Conversion," Phys. Rev. Lett. 100, 183601 (2008).
[84] H.G. de Chatellus, A.V. Sergienko, B.E.A. Saleh, M.C. Teich, and G. Di Giuseppe, "Non-collinear and Non-degenerate Polarization-Entangled Photon Generation Via Concurrent Type-I Parametric Downconversion in PPLN," Opt. Express 14, 10060–10072 (2006).
[85] M. Pysher, A. Bahabad, P. Peng, A. Arie, and O. Pfister, "Quasi-Phase-Matched Concurrent Nonlinearities in Periodically Poled $KTiOPO_4$ for Quantum Computing Over the Optical Frequency Comb," Opt. Lett. 35, 565–567 (2010).
[86] A. Christ, K. Laiho, A. Eckstein, T. Lauckner, P.J. Mosley, and C. Silberhorn, "Spatial Modes in Waveguided Parametric Down-Conversion," Phys. Rev. A 80, 033829 (2009).
[87] J.D. Bierlein, A. Ferretti, L.H. Brixner, and W.Y. Hsu, "Fabrication and Characterization of Optical Waveguides in KTiOPO4," Appl. Phys. Lett. 50, 1216 (1987).
[88] W.P. Risk, "Fabrication and Characterization of Planar Ion-Exchanged KTiOPO4 Waveguides for Frequency Doubling," Appl. Phys. Lett. 58, 19 (1991).
[89] A.S. Helmy, P. Abolghasem, J.S. Aitchison, B.J. Bijlani, J. Han, B.M. Holmes, D.C. Hutchings, U. Younis, and S.J. Wagner, "Recent Advances in Phase Matching of Second-Order Nonlinearities in Monolithic Semiconductor Waveguides," Laser Photonics Rev. 5, 272–286, 2011.
[90] R. Horn, P. Abolghasem, B.J. Bijlani, D. Kang, A.S. Helmy, and G. Weihs, "Monolithic Source of Photon Pairs," Phys. Rev. Lett. 108, 153605 (2012).
[91] M. Ravaro, Y. Seurin, S. Ducci, G. Leo, V. Berger, A. De Rossi, and G. Assanto, "Nonlinear AlGaAs Waveguide for the Generation of Counterpropagating Twin Photons in the Telecom Range," J. Appl. Phys. 98, 063103 (2005).

[92] L. Lanco, S. Ducci, J.-P. Likforman, X. Marcadet, J.A.W. van Houwelingen, H. Zbinden, G. Leo, and V. Berger, "Semiconductor Waveguide Source of Counterpropagating Twin Photons," Phys. Rev. Lett. 97, 173901 (2006).
[93] S. Tanzilli, H. De Riedmatten, W. Tittel, H. Zbinden, P. Baldi, M. De Micheli, D.B. Ostrowsky, and N. Gisin, "Highly Efficient Photon-Pair Source Using Periodically Poled Lithium Niobate Waveguide," Electron. Lett. 37, 26–28 (2001).
[94] K. Banaszek, A.B. U'Ren, and I.A. Walmsley, "Generation of Correlated Photons in Controlled Spatial Modes by Downconversion in Nonlinear Waveguides," Opt. Lett. 26, 1367 (2001).
[95] A.B. U'Ren, C. Silberhorn, K. Banaszek, and I. Walmsley, "Efficient Conditional Preparation of High-Fidelity Single Photon States for Fiber-Optic Quantum Networks," Phys. Rev. Lett. 93, 093601 (2004).
[96] P. Aboussouan, O. Alibart, D.B. Ostrowsky, P. Baldi, and S. Tanzilli, "High-Visibility Two-Photon Interference at a Telecom Wavelength Using Picosecond-Regime Separated Sources," Phys. Rev. A 81, 021801 (2010).
[97] S. Krapick, H. Herrmann, V. Quiring, B. Brecht, H. Suche, and C. Silberhorn, "An Efficient Integrated Two-Color Source for Heralded Single Photons," New J. Phys. 15, 033010 (2013).
[98] T. Zhong, X. Hu, F.N.C. Wong, K.K. Berggren, T.D. Roberts, and P. Battle, High-Quality Fiber-Optic Polarization Entanglement Distribution at 1.3 μm Telecom Wavelength," Opt. Lett. 35, 1392–1394 (2010).
[99] J. Chen, A.J. Pearlman, A. Ling, J. Fan, and A.L. Migdall, "A Versatile Waveguide Source of Photon Pairs for Chip-Scale Quantum Information Processing," Opt. Express 17, 6727–6740 (2009).
[100] A. Eckstein, A. Christ, P.J. Mosley, and C. Silberhorn, "Highly Efficient Single-Pass Source of Pulsed Single-Mode Twin Beams of Light," Phys. Rev. Lett. 106, 013603 (2011).
[101] T. Zhong, F.N.C. Wong, A. Restelli, and J.C. Bienfang, "Efficient Single-Spatial-Mode Periodically-Poled
KTiOPO4 Waveguide Source for High-Dimensional Entanglement-Based Quantum Key Distribution," Opt. Express 20, 26868–26877 (2012).
[102] G. Harder, V. Ansari, B. Brecht, T. Dirmeier, C. Marquardt, and C. Silberhorn, "An Optimized Photon Pair Source for Quantum Circuits," Opt. Express 21, 13975–13985 (2013).
[103] J.Ĺ. Svozilăk, M. Hendrych, A.S. Helmy, and J.P. Torres, "Generation of Paired Photons in a Quantum Separable State in Bragg Reflection Waveguides," Opt. Express 19, 3115–3123 (2011).
[104] M.C. Booth, M. Atatüre, Di Giuseppe, B.E.A. Saleh, A.V. Sergienko, and M.C. Teich, "Counterpropagating Entangled Photons from a Waveguide with Periodic Nonlinearity," Phys. Rev. A 66, 023815 (2002).
[105] M.F. Saleh, B.E.A. Saleh, and M.C. Teich, "Modal, Spectral, and Polarization Entanglement in Guided-Wave Parametric Down-Conversion," Phys. Rev. A (At. Mol. Opt. Phys.) 79, 053842–053852 (2009).
[106] P.J. Mosley, A. Christ, A. Eckstein, and C. Silberhorn, "Direct Measurement of the Spatial-Spectral Structure of Waveguided Parametric Down-Conversion," Phys. Rev. Lett. 103, 233901 (2009).
[107] M. Karpinski, C. Radzewicz, and K. Banaszek, "Experimental Characterization of Three-Wave Mixing in a Multimode Nonlinear $KTiOPO_4$ Waveguide," Appl. Phys. Lett. 94, 181105–181108 (2009).
[108] M. Fiorentino, S.M. Spillane, R.G. Beausoleil, T.D. Roberts, P. Battle, and M.W. Munro, "Spontaneous Parametric Down-Conversion in Periodically Poled KTP Waveguides and Bulk Crystals," Opt. Express 15, 7479–7488 (2007).
[109] S.M. Spillane, M. Fiorentino, and R.G. Beausoleil, "Spontaneous Parametric Down Conversion in a Nanophotonic Waveguide," Opt. Express 15, 8770–8780 (2007).
[110] J.M. White, and P.F. Heidrich, "Optical Waveguide Refractive Index Profiles Determined from Measurement of Mode Indices: A Simple Analysis," Appl. Opt. 15, 151–155 (1976).
[111] D. Marcuse, "Theory of Dielectric Optical Waveguides," Academic Press (1974).
[112] T.B. Koch, J.B. Davies, and D. Wickramasinghe, "Finite Element/Finite Difference Propagation Algorithm for Integrated Optical Device," Electron. Lett. 25, 514–516 (1989).
[113] B.C. Jacobs, T.B. Pittman, and J.D. Franson, "Single Photon Source Using Laser Pulses and Two-Photon Absorption," Phys. Rev. A 74, 010303 (2006).

[114] A. Christ, C. Silberhorn, "Limits on the Deterministic Creation of Pure Single-Photon States Using Parametric Down-Conversion." Phys. Rev. A 85, 023829–023835 (2012).
[115] U'Ren, K. Banaszek, and I.A. Walmsley, "Photon engineering for Quantum Information Processing." Quantum Info. Comput. 3, 480–502 (2003).